Reynolds number effect on statistics of turbulent flows over periodic hills ^{EP}

Zhideng Zhou (周志登), Ting Wu (吴霆) and Xiaolei Yang (杨晓雷)

COLLECTIONS

EP   This paper was selected as an Editor's Pick

View Online   Export Citation   CrossMark

ARTICLES YOU MAY BE INTERESTED IN

Wall-attached structures over a traveling wavy boundary: Scalar transport
Physics of Fluids **33**, 105115 (2021); https://doi.org/10.1063/5.0065449

Direct numerical simulation of turbulent channel flow up to $Re_\tau = 590$
Physics of Fluids **11**, 943 (1999); https://doi.org/10.1063/1.869966

Rotational and reflectional equivariant convolutional neural network for data-limited applications: Multiphase flow demonstration
Physics of Fluids **33**, 103323 (2021); https://doi.org/10.1063/5.0066049

Physics of Fluids

Special Topic: Food Physics

Submit Today!

AIP Publishing

33, 105124

Reynolds number effect on statistics of turbulent flows over periodic hills (EP)

View Online   Export Citation   CrossMark

Zhideng Zhou (周志登),[1,2] (iD) Ting Wu (吴霆),[1,2] (iD) and Xiaolei Yang (杨晓雷)[1,2,a] (iD)

AFFILIATIONS

[1]The State Key Laboratory of Nonlinear Mechanics, Institute of Mechanics, Chinese Academy of Sciences, Beijing 100190, China
[2]School of Engineering Sciences, University of Chinese Academy of Sciences, Beijing 100049, China

[a]Author to whom correspondence should be addressed: xyang@imech.ac.cn

ABSTRACT

The wall-resolved large-eddy simulations of turbulent flows over periodic hills are carried out to study the Reynolds number effect on flow statistics. Five different Reynolds numbers ranging from 2800 to 37 000 are considered. The present simulations are validated by comparing the time-averaged flow statistics with those from the literature. The Reynolds number effect is first examined on the skin friction and pressure coefficients, the isosurfaces of p' and Q criteria, and the vertical profiles of flow statistics. The results show that (1) at most locations the magnitude of friction coefficient decreases with the increase in Reynolds number, while the pressure coefficient varies in the opposite direction; (2) smaller turbulence structures arise at higher Reynolds numbers; and (3) the mean velocities and Reynolds stresses in general exhibit asymptotic behaviors with the increase in Reynolds number. The statistical properties of turbulence structures are further examined via the probability density function and time correlation of velocity fluctuations. At last, the dynamics in the separation bubble is investigated by examining the flow statistics and the budget equation of mean kinetic energy (MKE) on the coordinate with its origin fixed at the recirculation center, and the power spectral density of the velocity fluctuations. Similarities are in general observed for the mean velocities, Reynolds stresses, and the MKE budget in the rear part of the separation bubble. The mean convection term and turbulence convection term are observed playing a key role on the decrease in bubble size with the increase in Reynolds number.

I. INTRODUCTION

Separation and reattachment occur in many environmental and industrial flows at high Reynolds numbers, for example, underwater vehicle, fuselages at high incidence, curved ducts, and stalled wings and turbine blades. Their characteristics and mechanisms depending on case-specific initial and boundary conditions are not well understood yet. This poses a great challenge on developing wall models for large-eddy simulation (LES), which can significantly reduce the computational cost compared to direct numerical simulation (DNS) and has the potential to become the next-generation computational fluid dynamics tool for engineering designs.[1–4] The turbulent flows over periodic hills, which has all the essential flow features, is considered to be ideal for understanding the fundamental fluid dynamics and testing different wall models.[5,6] Studies of the periodic hill case have been carried out for different Reynolds numbers. The objective of this work is to systematically examine the effects of Reynolds number on turbulence statistics of the flow over periodic hills.

The flow over periodic hills, originally proposed by Almeida *et al.*[7] and modified by Mellen *et al.*,[8] is featured by separation from a curved surface, re-circulation, reattachment, and strong pressure gradient in the streamwise direction, which has been employed to test the accuracy of numerical methods[9–12] and turbulence models[5,13–15] and gain physical insight into separated turbulent flows.[16–18] Throughout this paper, the Reynolds number is defined as $Re_h = \rho U_b h/\mu$, where U_b is the bulk velocity, h is the height of the hill, ρ is the fluid density, and μ is the dynamic viscosity. Experiments have been carried out in the literature to provide experimental data for the development and validation of computational models. Breuer *et al.*[16] carried out measurements in a water channel at $Re_h \approx 5600$ and $10\,595$ using the particle image velocimetry (PIV) technique. Rapp and Manhart[19] undertook the two-dimensional PIV measurements in a water channel at four different Reynolds numbers in the range of $5600 \le Re_h \le 37\,000$, with validation using the point-by-point one-dimensional laser Doppler anemometry (LDA) measurements. Kahler *et al.*[20] performed the high-resolution PIV and particle tracking velocimetry (PTV) measurements in a water tunnel at Reynolds numbers of 8000 and 33 000 at a spatial resolution comparable to that of DNS, which provides database for a precise analysis of the near-wall flow features.

Different numerical methods have been employed in the literature to study the turbulence statistics of the flow over periodic hills. DNS was employed by Breuer et al.,[16] Balakumar,[21] Krank et al.,[17] and Xiao et al.[22] for the flow at Reynolds numbers of $100 \leq Re_h \leq 10\,595$. In most studies,[5,6,16,23] wall-resolved large-eddy simulation (WRLES) solving the incompressible Navier–Stokes equations was employed with a finite difference/finite volume method of second-order accuracy for the spatial discretization. A compressible solver was employed by Ziefle et al.[24] and Balakumar.[21] High-order discretization schemes were employed by Balakumar,[21] Krank et al.,[17] and Gloerfelt and Cinnella.[18] In the work by Temmerman et al.[5] and Ziefle et al.,[24] different subgrid-scale (SGS) models were tested. To date, the highest Reynolds number carried out using WRLES is $Re_h = 37\,000$. Using wall-modeled large-eddy simulation (WMLES), the periodic hill case at $Re_h = 10^5$ was carried out by Gao et al.[23]

Since flows in realistic applications often happen at much higher Reynolds numbers, it is of vital importance to understand how Reynolds number affects the statistics of the turbulent flows over periodic hills, which influences how well we can apply the knowledge obtained at low Reynolds numbers to cases at high Reynolds numbers and the extrapolation properties of data-driven models trained using data from cases at low Reynolds numbers.[25] Breuer et al.[16] numerically and experimentally investigated the flow over periodic hills with Reynolds number in the range of $100 \leq Re_h \leq 10\,595$. It was observed that both the separation and reattachment locations move upstream with increasing Re_h, while the former one reaches its minimum at $Re_h = 5600$ and then increases, and the latter one shows a local minimum at $Re_h = 2800$. Based on observations on the instantaneous flow structures, they found that the flow state changes from steady to unsteady at approximately $Re_h = 200$. Rapp and Manhart[19] compared the vertical profiles of mean velocities and Reynolds stresses measured in a water channel for Reynolds numbers $Re_h = 5600, 10\,600, 19\,000, 37\,000$. They found that the recirculation zone behind the hill flattens and the reattachment position moves upstream with increasing Re_h. Recently, Gao et al.[23] investigated the Reynolds number effects on the dynamics inside the recirculation zone using WMLES for Reynolds number up to $Re_h = 10^5$. It was found that the length of the separation bubble behind the hill decreases with Re_h. In addition to the flow over periodic hills, there are various studies about the Reynolds number effect on the flow separation for different flows. Song and Eaton[26] performed experiments of a separating, reattaching, and recovering boundary layer in the closed-loop wind tunnel mounted inside a pressure vessel and proposed empirical Reynolds number scalings for the mean velocity and Reynolds stresses for different flow regions. They found that the mean flow is a weak function of Reynolds number, while turbulence quantities strongly depend on Reynolds number. Abe[27] examined DNS datasets of a pressure-induced turbulent separation bubble on a flat plate in which the Reynolds number effects on wall-pressure fluctuations, power spectra, and instantaneous fields were investigated. It was observed that the mean velocities and Reynolds stresses are dependent on the Reynolds number, but the scaling law of wall-pressure fluctuation near reattachment is attained independently of the Reynolds number and pressure gradient. Later, the effects of Reynolds number and pressure gradient on the momentum transport were studied by Abe[28] for the same flow. Coleman et al.[29] performed DNS of a family of separation bubbles by varying the severity of pressure gradients and the Reynolds number, and investigated

the Reynolds number dependence of skin-friction in different flow regions. It is noted that these studies on Reynolds number effects are mainly limited to the time-averaged velocities, Reynolds stresses, and the separation and reattachment locations.

In this work, we first give a comprehensive comparison of flow statistics between the previous experimental and numerical studies (DNS and WRLES) and the present WRLES results of turbulent flows over periodic hills in the range of $Re_h = 2800 \sim 37\,000$. Then, the effects of Reynolds number on the global flow features, instantaneous turbulence structures, and statistical properties are systematically examined. At last, the dynamics and Reynolds number effects are investigated for the separation bubble by analyzing the flow statistics and the budget of mean kinetic energy (MKE) on the coordinate with its origin fixed at the bubble, and the power spectral density of velocity fluctuations.

In the rest of the paper, the methodology and the case setups are described in Sec. II. In Sec. III, the present simulation results are validated using data from the literature. Then, the Reynolds number effects are systematically analyzed in Sec. IV. At last, conclusions from this study are drawn in Sec. V.

II. METHODOLOGY

In this section, we describe the employed numerical method and the simulation setup for the WRLES cases carried out in this work.

A. Numerical method

We employ the Virtual Flow Simulator (VFS-Wind)[30,31] code for WRLES of turbulent flows over periodic hills. The VFS code has been successfully applied to industrial and environmental turbulent flows.[32–39] In VFS-Wind code, the governing equations are the three-dimensional unsteady spatially filtered incompressible Navier–Stokes equations in non-orthogonal, generalized curvilinear coordinates shown as follows:

$$J \frac{\partial U^j}{\partial \xi^j} = 0,$$

$$\frac{1}{J}\frac{\partial U^i}{\partial t} = \frac{\xi^i_l}{J}\left(-\frac{\partial}{\partial \xi^j}(U^j u_l) - \frac{1}{\rho}\frac{\partial}{\partial \xi^j}\left(\frac{\xi^j_l p}{J}\right) \right.$$
$$\left. + \frac{\mu}{\rho}\frac{\partial}{\partial \xi^j}\left(\frac{g^{jk}}{J}\frac{\partial u_l}{\partial \xi^k}\right) - \frac{1}{\rho}\frac{\partial \tau_{lj}}{\partial \xi^j} \right), \quad (1)$$

where x_i and ξ^i are the Cartesian and curvilinear coordinates, respectively; $\xi^i_l = \partial \xi^i / \partial x_l$ are the transformation metrics; J is the Jacobian of the geometric transformation; u_i is the ith component of the velocity vector in Cartesian coordinates; $U^i = (\xi^i_m/J)u_m$ is the contravariant volume flux; $g^{jk} = \xi^j_l \xi^k_l$ are the components of the contravariant metric tensor; and p is the pressure. In the momentum equation, τ_{ij} represents the anisotropic part of the subgrid-scale stress tensor, which is modeled by the Smagorinsky model,

$$\tau_{ij} - \frac{1}{3}\tau_{kk}\delta_{ij} = -2\nu_t \bar{S}_{ij}, \quad (2)$$

where $\bar{S}_{ij} = \frac{1}{2}\left(\frac{\partial U_i}{\partial x_j} + \frac{\partial U_j}{\partial x_i}\right)$ is the filtered strain-rate tensor and ν_t is the eddy viscosity calculated by

$$\nu_t = C\Delta^2 |\bar{S}|, \quad (3)$$

where C is the model coefficient calculated dynamically using the procedure of Germano et al.,[40] $|\bar{S}| = \sqrt{2\bar{S}_{ij}\bar{S}_{ij}}$ and $\Delta = J^{-1/3}$ is the filter size, where J^{-1} is the cell volume.

The governing equations are spatially discretized using a second-order accurate central differencing scheme and integrated in time using the fractional step method. An algebraic multigrid acceleration along with generalized minimal residual method (GMRES) solver is used to solve the pressure Poisson equation. A matrix-free Newton–Krylov method is used for solving the discretized momentum equation. More details about the flow solver can be found in the literature.[30,41,42]

B. Simulation setup

The geometry of the periodic hills is shown in Fig. 1. As seen, the height of the hill is h, a flat plate is placed $2.036h$ above the crest of the hill and the distance between the crests of two hills is $L_x = 9h$. In the spanwise direction, the size of the computational domain is $L_z = 4.5h$. The bulk velocity is defined as $U_b = Q/(\rho L_z \times (L_y - h))$, where Q is the mass flux. No-slip boundary condition is applied at the top wall and the surface of the hills. In the streamwise and spanwise directions, periodic boundary condition is applied. The flow is driven by a pressure gradient uniformly applied to whole domain to maintain a constant mass flux.

The computational domain is discretized using a body-fitted curvilinear grid (as shown in Fig. 1). Five different Reynolds numbers, that is, $Re_h = 2800, 5600, 10\,595, 19\,000, 37\,000$, are considered as listed in Table I. The simulation is first carried out for about $22T$ (flow-through time $T = L_x/U_b$) for the flow to achieve a fully developed state. Then, the flow is further advanced for about $50T$ for time-averaged quantities.

To evaluate the quality of the employed body-fitted curvilinear grid, we examine the distributions of wall-normal grid size in wall unit Δy^+ defined as $\Delta y^+ = \Delta y_c u_\tau/\nu$, where $u_\tau = \sqrt{\tau_w/\rho}$ denotes the local friction velocity, τ_w denotes the wall shear stress, and $\nu = \mu/\rho$ denotes the kinematic viscosity, and the streamwise grid size in wall unit Δx^+ is defined in a similar way. As seen in Fig. 2, the cell sizes in the streamwise direction are in general below 20 wall units. As for
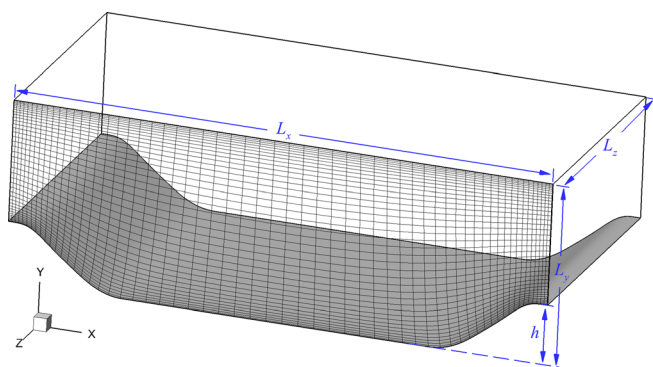
FIG. 1. Schematic of the periodic hills, computational domain ($L_x = 9.0h$, $L_y = 3.036h$, $L_z = 4.5h$), and the employed curvilinear mesh on a x–y plane at $Re_h = 10\,595$ (on which every fifth grid line is displayed).

TABLE I. Parameters of the WRLES of flow over periodic hills.

Case	Re_h	Mesh ($N_x \times N_y \times N_z$)	$\Delta t \cdot U_b/h$	$\Delta y_c^{\,a}/h$
1	2800	$297 \times 193 \times 187$	0.01	0.0015
2	5600	$297 \times 193 \times 187$	0.01	0.0015
3	10 595	$297 \times 193 \times 187$	0.01	0.0015
4	19 000	$460 \times 300 \times 290$	0.005	0.00075
5	37 000	$759 \times 493 \times 477$	0.0025	0.0005

$^a\Delta y_c$ denotes the distance of the center of the first off-wall cell from the wall.

Δy^+, the values of Δy^+ are approximately below 0.5 except for the windward and the crest of the hill for $Re_h = 10\,595$–$37\,000$.

The temporal series of the three components of the velocity and the pressure on four different $x - y$ slices are saved for subsequent analyses. The temporal increment between two successive snapshots is $0.01h/U_b$ for all cases. The spanwise spacing between two neighbor slices is $1.125h$. At the two boundaries at $z/h = 0$ and $z/h = 4.5$, only the data on the slice located at $z/h = 0$ are saved considering the periodic boundary condition applied in the spanwise direction. For the cases with $Re_h = 2800, 5600, 10\,595$, 45 000 snapshots are saved. For the cases with $Re_h = 19\,000, 37\,000$, 22 500 and 11 300 snapshots are saved, respectively.

III. VALIDATION

In this section, we compare the flow statistics computed in this work with the reference data. Before presenting the comparison results, we first show in Fig. 3 the contour of the streamwise velocity with streamlines at $Re_h = 37\,000$ to showcase the typical flow structure for the flow over periodic hills. In the figure, the center of the recirculation zone is located at the intersection of the isolines with the zero mean streamwise and vertical velocities. Then, the flow quantities on the streamwise and vertical profiles through the center of the recirculation zone are extracted and compared on the coordinate with its origin fixed at the recirculation center in Sec. IV D. Figures 4 and 5 show the comparison at ten different streamwise stations located at $x/h = 0.05$, 0.5, 1, 2, 3, 4, 5, 6, 7, 8 for four different Reynolds numbers. In the horizontal axis, the bracket $\langle \rangle$ denotes the ensemble average of the flow quantities over time and the spanwise direction. The data employed for comparison include the DNS data of Krank et al.[17] at $Re_h = 5600, 10\,595$, the WRLES data of Gloerfelt and Cinnella[18] at $Re_h = 10\,595, 19\,000, 37\,000$, and the PIV measurements of Rapp and Manhart[19] at all four different Reynolds numbers. The results from the present simulations agree well with the DNS and measured data for all quantities at different streamwise locations with the relative error less than 5% for all the four different Reynolds numbers except for certain components of the Reynolds stress at $Re_h = 5600$ and 37 000. The major differences are observed between the computed results and measurements at the upper part of profile $x/h = 0.05$ -2.0 and lower part of profile $x/h = 2.0 \sim 6.0$ for $\langle u'u' \rangle$ for the case with $Re_h = 5600$, and the lower part of profile $x/h = 0.05$–6.0 for $\langle v'v' \rangle$ for the case with $Re_h = 37\,000$, respectively. It is seen that the results from the present simulation and those from the simulation in the literature agree well with each other. This indicates that such differences are possibly caused by the uncertainty of the experiment, which can be justified by plotting the measured $\langle u'u' \rangle$ or $\langle v'v' \rangle$ from
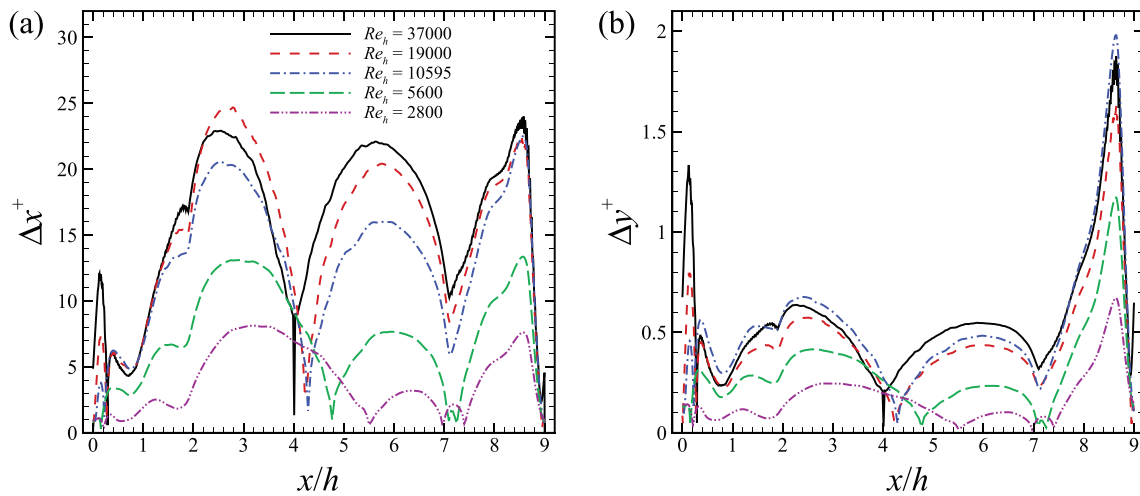
FIG. 2. Distribution of (a) Δx^+ and (b) Δy^+ along the bottom wall for cases with different Reynolds numbers.

different Reynolds numbers (not shown in this paper), showing that the measured values of $\langle u'u' \rangle$ and $\langle v'v' \rangle$ are off the trend at those locations for $Re_h = 5600$ and $Re_h = 37\,000$, respectively.

IV. RESULTS

A. Global flow features

In this section, we examine the dependence of some global flow features on Reynolds number. In Fig. 6, we evaluate the effects of Reynolds number on the skin friction and pressure coefficients, which are defined as follows:

$$C_f = \frac{\langle \tau_w \rangle}{\frac{1}{2}\rho U_b^2}, \quad C_p = \frac{\langle p \rangle - p_{\text{ref}}}{\frac{1}{2}\rho U_b^2}, \quad (4)$$

where p is the pressure and p_{ref} is the reference pressure at $x = 0$ on the bottom wall. Figure 6 displays the distributions of skin friction and pressure coefficients along the bottom wall. It is seen that the magnitude of both the maximum C_f at the windward of the hill
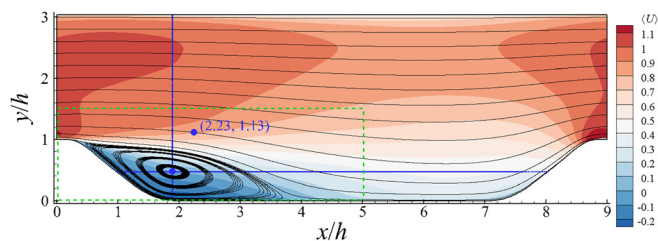

FIG. 3. Contour of time-averaged streamwise velocity with streamlines from the WRLES case at $Re_h = 37\,000$. Two points are extracted from the flow fields at different Re_h, the first one is the center of the recirculation zone, and the second one is located at $x/h = 2.23$, $y/h = 1.13$ in the shear layer. According to the coordinate of the first point, the flow quantities on the blue, solid lines along the x and y axes are extracted for comparison, and the green, dashed rectangle denotes the range of flow field that we concerned.

(at $x/h \approx 8.5$) and the minimum C_f in the recirculation zone (at $x/h \approx 2 \sim 5$) decreases with the increase in Reynolds number. Interestingly, the second maximum C_f, which is close to the separation location, increases monotonously with the Reynolds number.

In Fig. 6(c), the pressure coefficients from cases of different Reynolds numbers are compared. First of all, it is observed that the pressure gradients computed from the present cases agree well with the DNS results.[17] For the comparison between different Reynolds numbers, it is seen that the magnitudes of pressure coefficient increase monotonously with Reynolds number until $Re_h = 19\,000$, and does not change significantly by further increasing the Reynolds number to $Re_h = 37\,000$.

Figure 7 shows the variations of the separation and reattachment locations via Reynolds number with the results from the literature. When compared with the results from the literature, differences are observed for both separation and reattachment locations, which highlights the difficulty to accurately predict them, although good agreements are observed for the vertical profiles of mean velocity and Reynolds stresses (Figs. 4 and 5). There are two reasons for such differences: (1) the complex dynamics involved near the separation and reattachment points that a small change in the incoming turbulence or pressure gradient can alter the location where separation or reattachment occurs; (2) the approach for determining these two location may introduce errors, for example, a 4% (of the maximum $cf.$) on the friction coefficient can introduce differences on the separation and reattachment points as high as 15%. Considering the sensitivity of these two points, differences less than 20% shown in Fig. 7 are acceptable. With the increase in the Reynolds number, the separation location moves downstream starting from $Re_h = 5600$, which confirms the finding by Breuer et al.[16] The reattachment location gradually moves upstream with the increase in Reynolds number for the considered cases, which supplements the observation for Reynolds number in the range of $2800 \leq Re_h \leq 10\,595$.[16]

In Fig. 8, we examine the vortex structures from cases with different Reynolds numbers, which are identified using the isosurface of p'
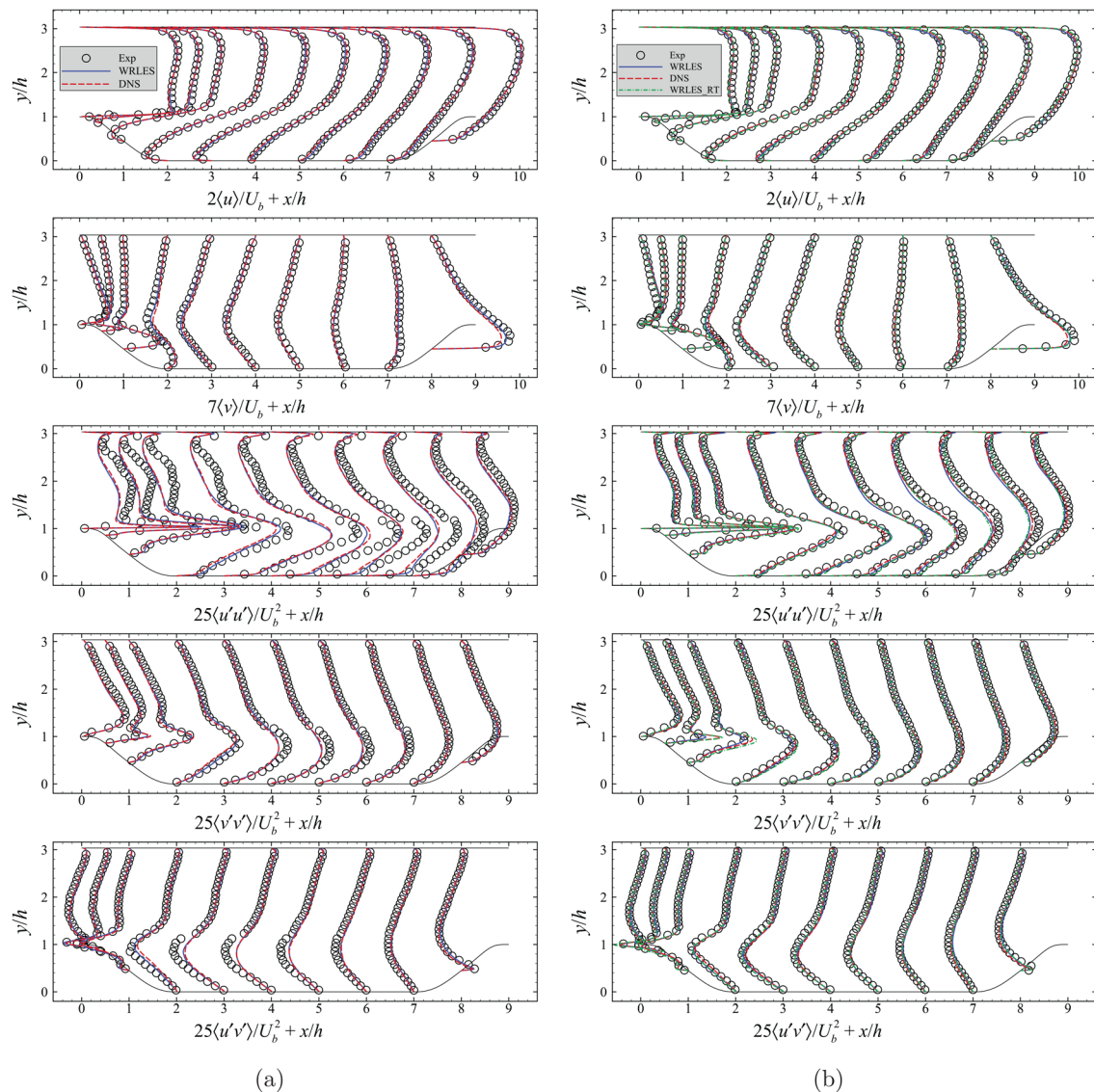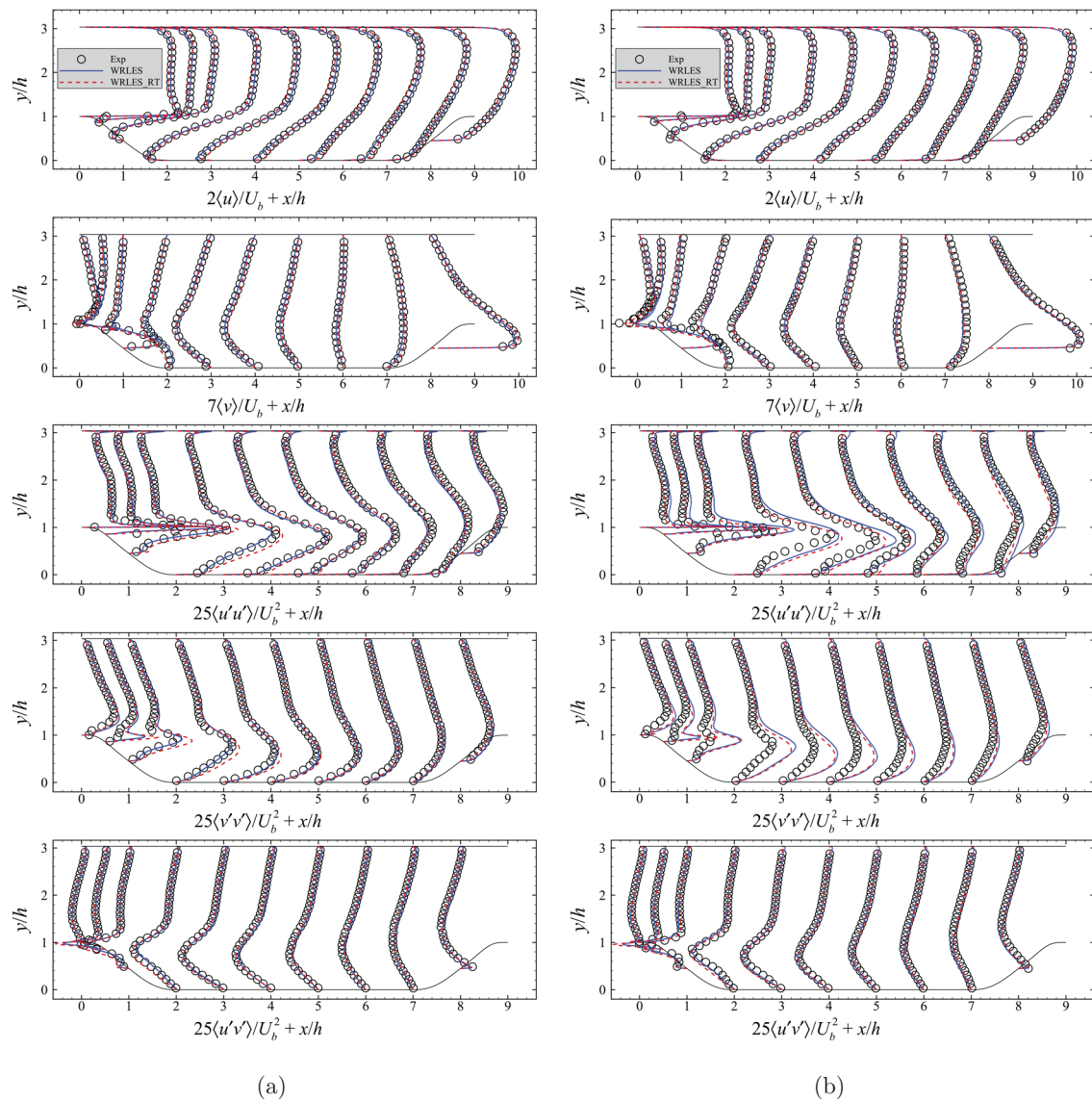
FIG. 4. Comparison of the vertical profiles obtained from the present WRLES with the DNS of Krank *et al.*,[17] the WRLES of Gloerfelt and Cinnella[18] (WRLES_RT, the LES with Regularization term strategy) and PIV measurements of Rapp and Manhart[19] for the mean streamwise velocity $\langle u \rangle$, the vertical velocity $\langle v \rangle$, and the Reynolds stress $\langle u'u' \rangle$ and $\langle v'v' \rangle$, and $\langle u'v' \rangle$ for (a) $Re_h = 5600$ and (b) $Re_h = 10\,595$.

and Q criteria and colored using the instantaneous streamwise velocity. Here, p' denotes the pressure fluctuation and Q denotes the second invariant of velocity gradient tensor.[6,17,43] As for the negative p' region, hairpin-like spanwise structures with the size in the spanwise dimension comparable to the spanwise width of the computational domain tend to emerge after the separation point. The spanwise structures become increasingly larger along the separated shear layer and form large-scale spanwise rollers above the recirculation zone, which were also observed in the backward facing step flow[44] and the turbulent boundary layers with adverse pressure gradient and separation.[27,45] Then, the spanwise structures break at further downstream locations and transform into inclined streamwise structures as approaching the

windward of the downstream hill. With the increase in Reynolds number, the number of small scales increases inside large scales, and the finer turbulent structures start to appear as identified by both Q and p' criteria.[27]

B. Comparison of mean profiles at typical streamwise locations

In this section, we examine the Reynolds number dependence of different flow statistics at four typical streamwise locations, that is, $x/h = 0.05, 2, 6, 8$ for the flow before separation with adverse pressure gradient, within the separation bubble, after reattachment and

FIG. 5. Comparison of the vertical profiles obtained from the present WRLES with the WRLES of Gloerfelt and Cinnella[18] and PIV measurements of Rapp and Manhart[19] for the mean streamwise velocity $\langle u \rangle$, the vertical velocity $\langle v \rangle$, and the Reynolds stress $\langle u'u' \rangle$ and $\langle v'v' \rangle$, and $\langle u'v' \rangle$ for (a) $Re_h = 19\,000$ and (b) $Re_h = 37\,000$.

before reaching the hill crest with positive pressure gradient, and different vertical locations.

Figure 9 shows the comparison at $x/h = 0.05$, the position just before flow separation. As seen, the boundary layer near the bottom wall is very thin with its thickness decreasing with the increase in the Reynolds number. The flow, which just accelerates from the windward of the hill, is featured by a peak in the streamwise velocity near the wall and a positive vertical velocity indicating an upward motion of the flow. With the increase in Reynolds number, an increase is observed on the magnitude of the peak of the streamwise velocity located near the hill surface with a decrease on the magnitude of the vertical velocity. For the normal Reynolds stresses, it is observed that

the peaks near the hill surface are significantly larger than those near the top wall. Interestingly, it is seen that the normal Reynolds stresses from different Reynolds numbers are very close to each other. Complicated variations are observed on the vertical profiles of the primary Reynolds shear stress $\langle u'v' \rangle$. Two peaks are observed near the hill surface, with the first peak located just next to the wall at $y/h \approx 1$ and the second peak located at $y/h \approx 1.5$. The magnitude of the first peak increases, while the magnitude of the second peak decreases with the increase in Reynolds number. The variation of $\langle u'v' \rangle$ is very different from that of the channel flow or the plenary boundary layer flows, indicating complex momentum transfer at this location and the challenge of wall modeling based on equilibrium hypothesis. Importantly,
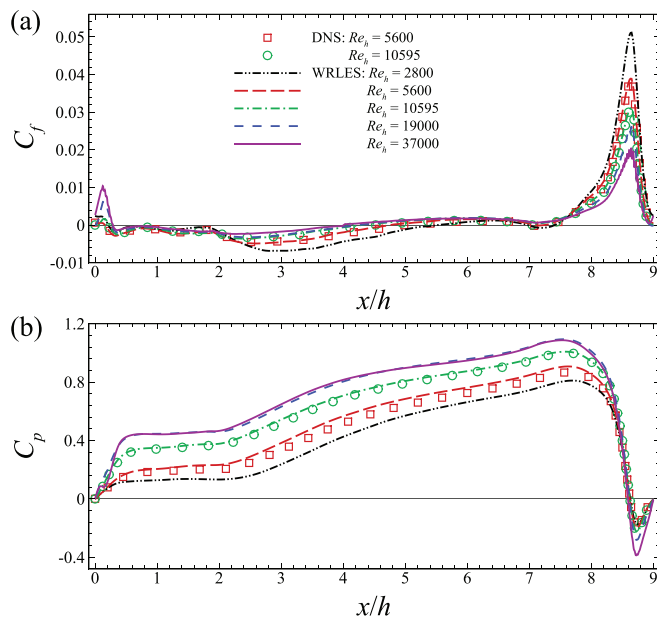
FIG. 6. Comparison of (a) the skin friction coefficient C_f and (b) pressure coefficient C_p along the bottom wall between the present WRLES and the DNS[17] for different Re_h.

it is observed that the profiles from the cases with $Re_h = 19\,000$, $37\,000$ are very close to each other indicating a certain degree of Reynolds number independence.

Figure 10 shows the comparison at $x/h = 2$ located within the recirculation zone. A recirculation zone is identified easily from the sign of the streamwise velocity, with a boundary layer appearing just above the hill surface within the recirculation zone. With the increase in Reynolds number, an asymptotic behavior is observed for the streamwise velocity. As moving away from the hill surface, the vertical
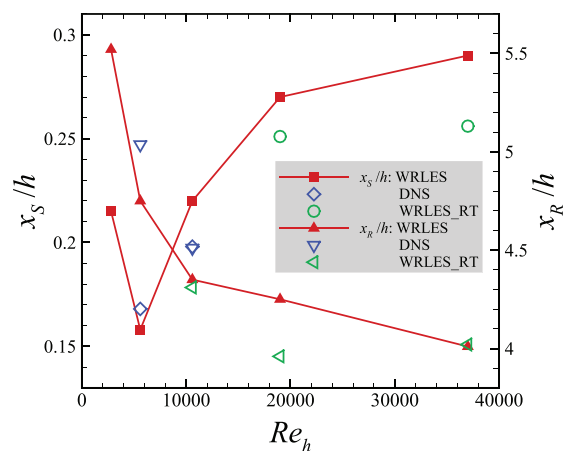
FIG. 7. Separation and reattachment locations predicted by the present WRLES, the WRLES_RT of Gloerfelt and Cinnella,[18] and the DNS of Krank et al.[17] at different Reynolds numbers.

velocity changes from positive to negative indicating upward motion and downward motion near the hill surface and above the recirculation bubble, respectively. The extent of the vertical motion deceases near the wall, while increases above the recirculation bubble, respectively, with the increase in the Reynolds number. As for Reynolds stresses, the overall distributions are similar for different Reynolds numbers. Differences are observed in terms of the value and location of the peaks of the Reynolds stresses. With the increase in Reynolds number, a clear asymptotic behavior is not observed for the Reynolds stresses.

Figure 11 shows the comparison at $x/h = 6$, the position just after the reattachment. At this position, the flow recovers from the recirculation zone with positive streamwise velocity and negative vertical velocity indicating a downward motion of flow. It is observed that the recovery rate of the streamwise velocity is increased with less level of downward motion as the increase in the Reynolds number. A clear asymptotic behavior is observed for the streamwise and vertical velocities except that differences between results at $Re_h = 19\,000$ and $Re_h = 37\,000$ are minor. Except for $Re_h = 2800$, the magnitude of the peak of the Reynolds stresses gradually decreases as the Reynolds number increases. The differences between the results from the cases with $Re_h = 19\,000$ and $Re_h = 37\,000$ are minor indicating asymptotic trends for the Reynolds stresses at this position.

Figure 12 shows the comparison at $x/h = 8$, which is located at the windward of the hill. It is seen that at this position, the flow is featured by an upward motion. This upward motion is enhanced with the increase in the Reynolds number. Decreases on the magnitudes of the peaks of the streamwise and vertical components of the normal Reynolds stresses are observed. Interestingly, it is observed that the magnitudes of the spanwise component of the Reynolds stresses are larger than the other two components, which is not observed in turbulent channel flows and plenary boundary layer flows. As for the primary Reynolds shear stress, two peaks are observed, one positive one located near the hill surface and the other negative one located away from the hill surface. With the increase in the Reynolds number, asymptotic behaviors are observed for both mean velocities and Reynolds stresses except for the spanwise component of the Reynolds stress.

C. Statistics of velocity fluctuations

After examining the Reynolds number effect on time-averaged velocity and Reynolds stresses, here we examine the probability density function (PDF) and time correlations of the velocity fluctuations for the whole computational domain, and the four different vertical locations, that is, at $\Delta y/h = 0.03, 0.1, 0.3$, and 1.0 away from the wall, are extracted for discussion. Figures 13–16 show the PDF of velocity and pressure fluctuations at $\Delta y/h = 0.03$ on the typical vertical profile $x/h = 0.05, 2.0, 6.0$, and 8.0, where σ denotes the standard deviation of the flow quantity. At this near-wall position, the PDFs are far from the Gaussian distribution. For the PDF of velocity fluctuation, the streamwise component exhibits negative deviation compared to the Gaussian distribution at vertical profile $x/h = 0.05$ and 2.0 due to the reversed flow, and exhibits positive deviation at vertical profile $x/h = 6.0$ and 8.0; the vertical component exhibits nearly symmetric distribution at vertical profile $x/h = 0.05$ before the flow separation, and then, the negative deviation arises from the flow separation at $x/h = 2.0$ and 6.0, and the deviation becomes positive at the windward of
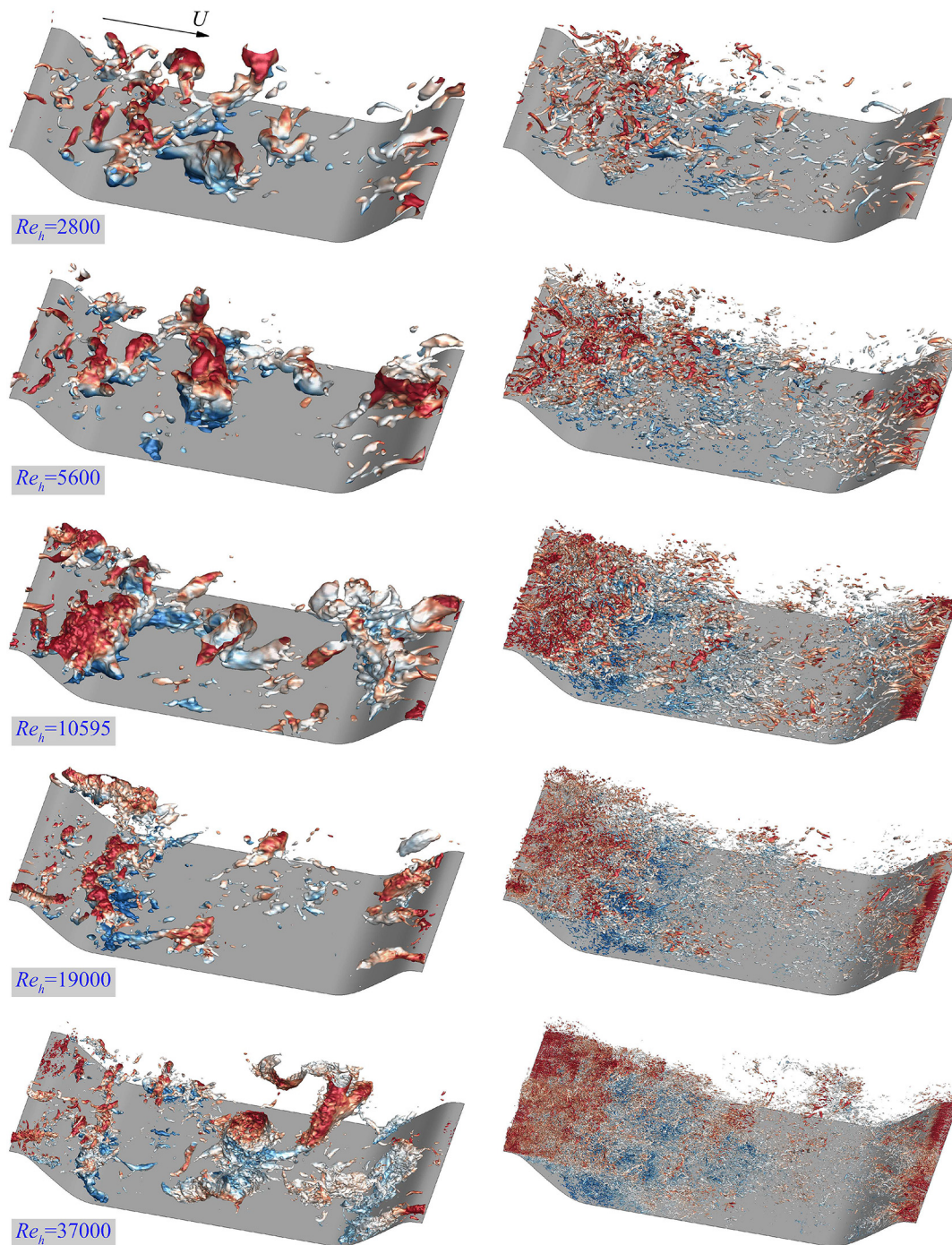
FIG. 8. Vortex structures identified using isosurface of instantaneous pressure fluctuations p' (left column) and Q (right column) for different Reynolds numbers.

the hill ($x/h = 8.0$); the spanwise component is almost symmetrical with the mean value of zero for all profiles. The PDF of pressure fluctuation shows good symmetry at $x/h = 2.0$ and 6.0, but exhibits significant positive deviation at $x/h = 8.0$ because of the raising of

pressure gradient at the windward slope of the hill. Interestingly, the PDF of vertical velocity fluctuation exhibits exponential distribution and the decay rate on the right are larger than the growth rate on the left at $x/h = 2.0$ and 6.0.
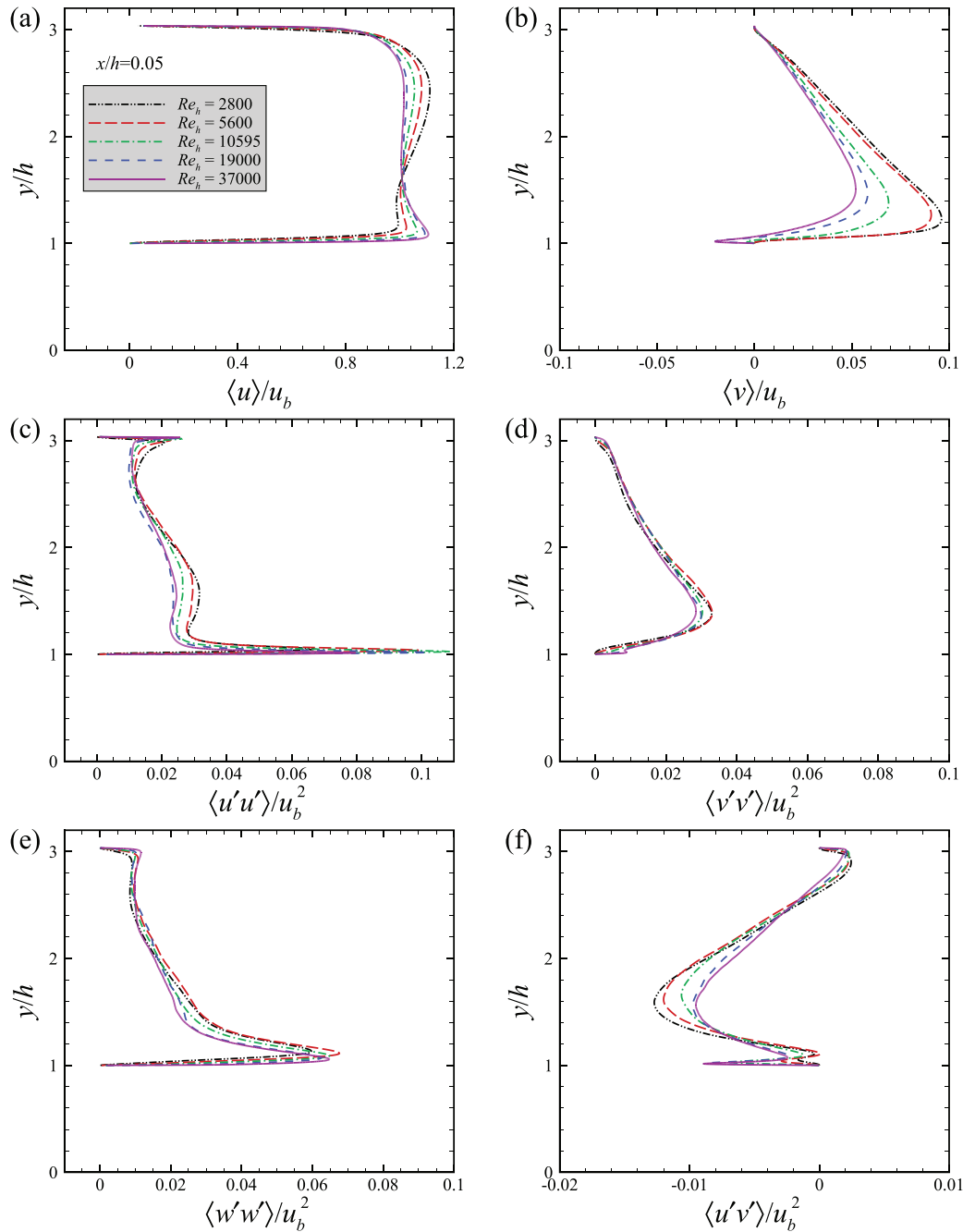
FIG. 9. Mean velocities (a and b) and Reynolds stresses (c–f) at $x/h = 0.05$.

To quantitatively measure the asymmetry and the deviation from the normal distribution of the PDF of the velocity fluctuations, we calculate the skewness and flatness factors of the PDF, which are defined as

$$S_x = \frac{\langle (x - \langle x \rangle)^3 \rangle}{\langle (x - \langle x \rangle)^2 \rangle^{3/2}}, \quad F_x = \frac{\langle (x - \langle x \rangle)^4 \rangle}{\langle (x - \langle x \rangle)^2 \rangle^2}. \quad (5)$$

Figures 17 and 18 plot the contours of the computed skewness and flatness factors of PDFs for velocity fluctuations on the x–y plane. The most important observation from these two figures is that the overall distributions of both skewness and flatness factors computed from cases with different Reynolds numbers are similar with each other, which is consistent with the similarity observed
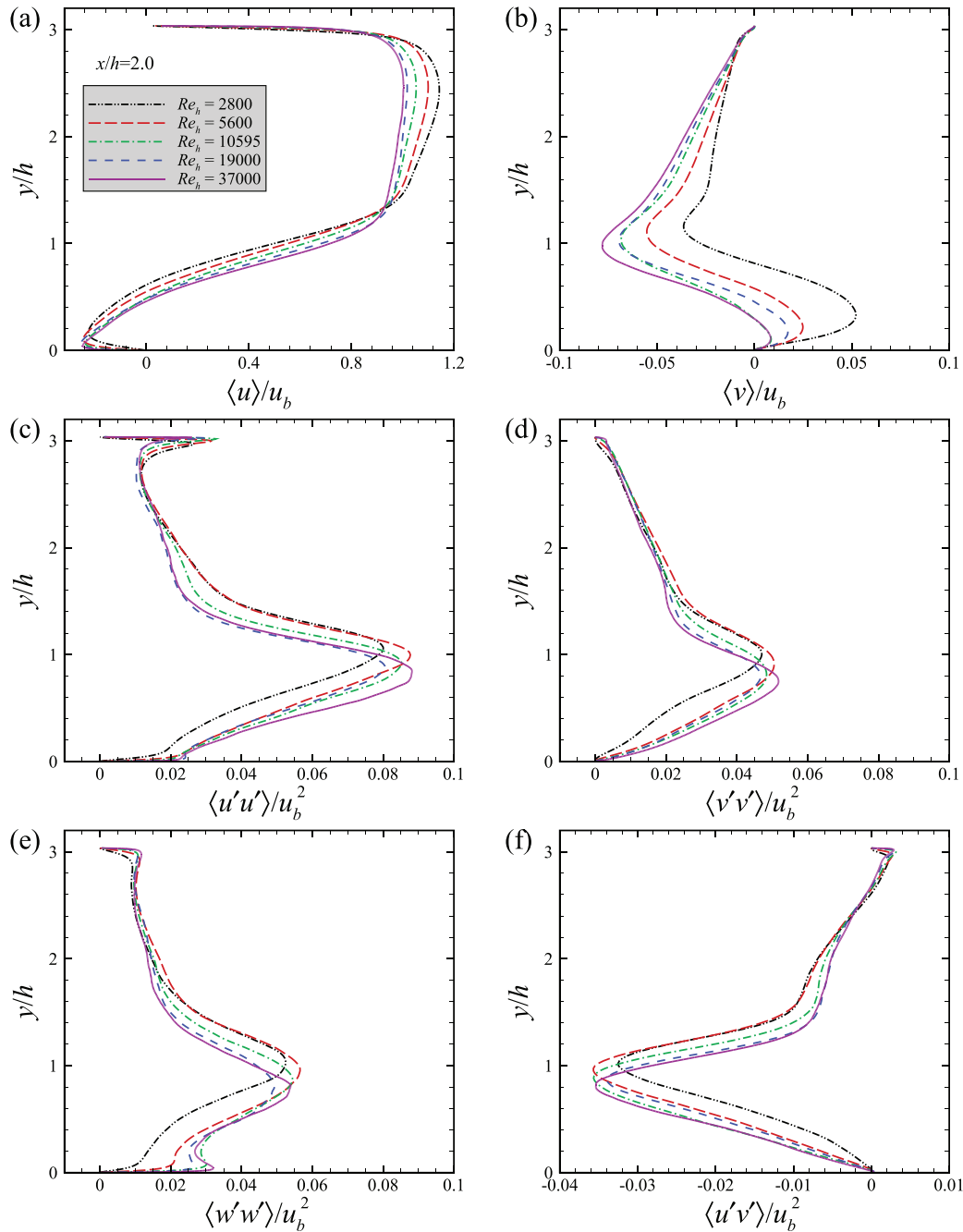
FIG. 10. Mean velocities (a and b) and Reynolds stresses (c–f) at $x/h = 2.0$.

on the turbulence structures shown in Fig. 8. Furthermore, it is observed that the skewness and flatness factors deviate differently from 0 and 3, which are the values for the Gaussian distribution, for different velocity components. For the spanwise velocity fluctuation, the skewness factors are approximately zero in nearly the whole region, and the flatness factors are close to three at most locations, indicating that the Gaussian distribution can approximate well the PDF of the spanwise velocity fluctuations. Even though the periodic boundary condition is applied in the spanwise direction, this is nontrivial considering the highly heterogeneous
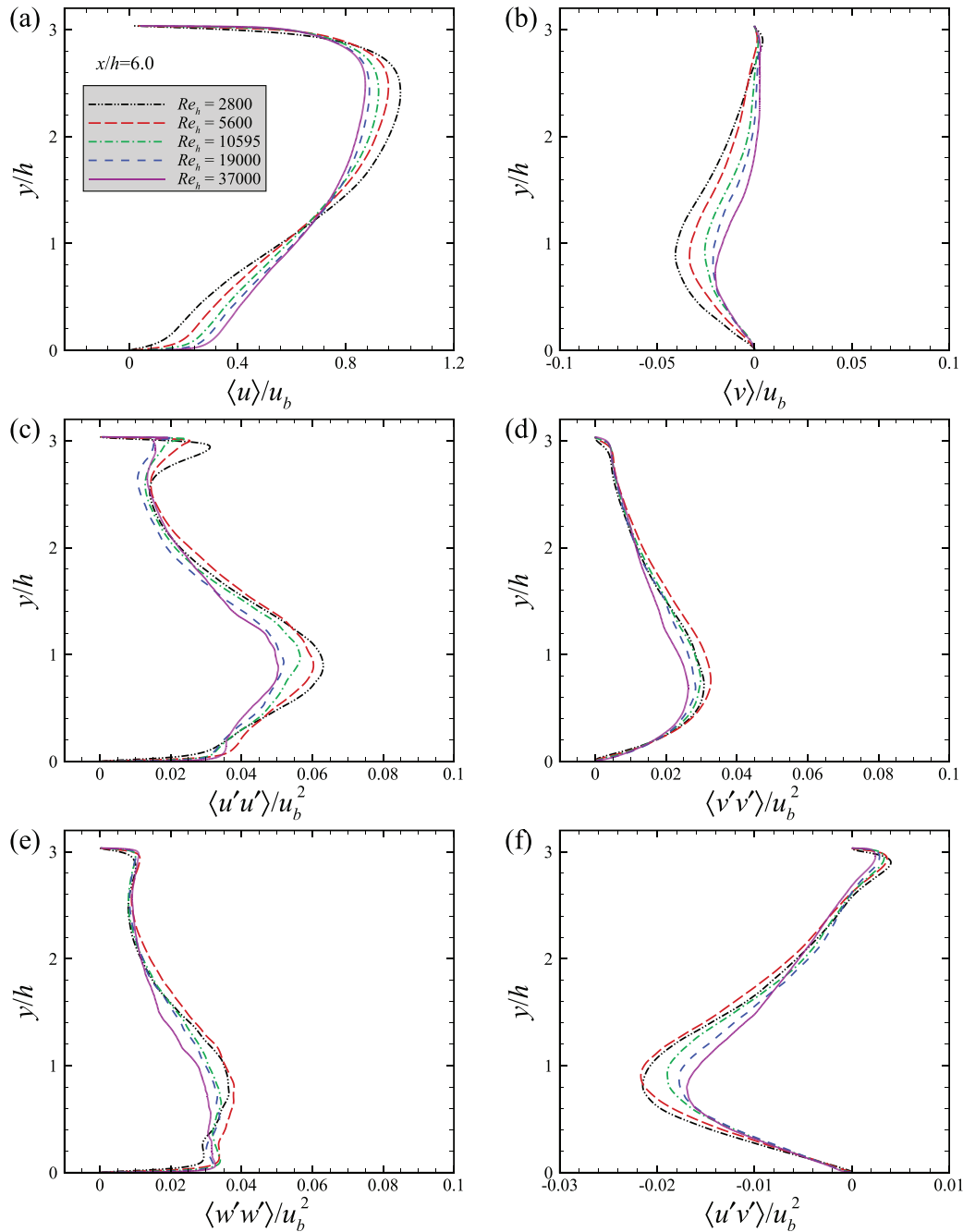
FIG. 11. Mean velocities (a and b) and Reynolds stresses (c–f) at $x/h = 6.0$.

flow field on the x–y plane. The skewness factors of the streamwise velocity fluctuations are less than zero in the region roughly extended slantwise from the hill crest to the center of channel, while these are greater than zero in a small region (without considering the size, it is roughly mirrored with the spanwise region with negative skewness factors) in the recirculation bubble and near the bottom and top walls, indicating positive and negative medians of the streamwise velocity fluctuations in the corresponding regions, respectively. The skewness factors of the vertical velocity fluctuations are distributed in an opposite way with positive and negative
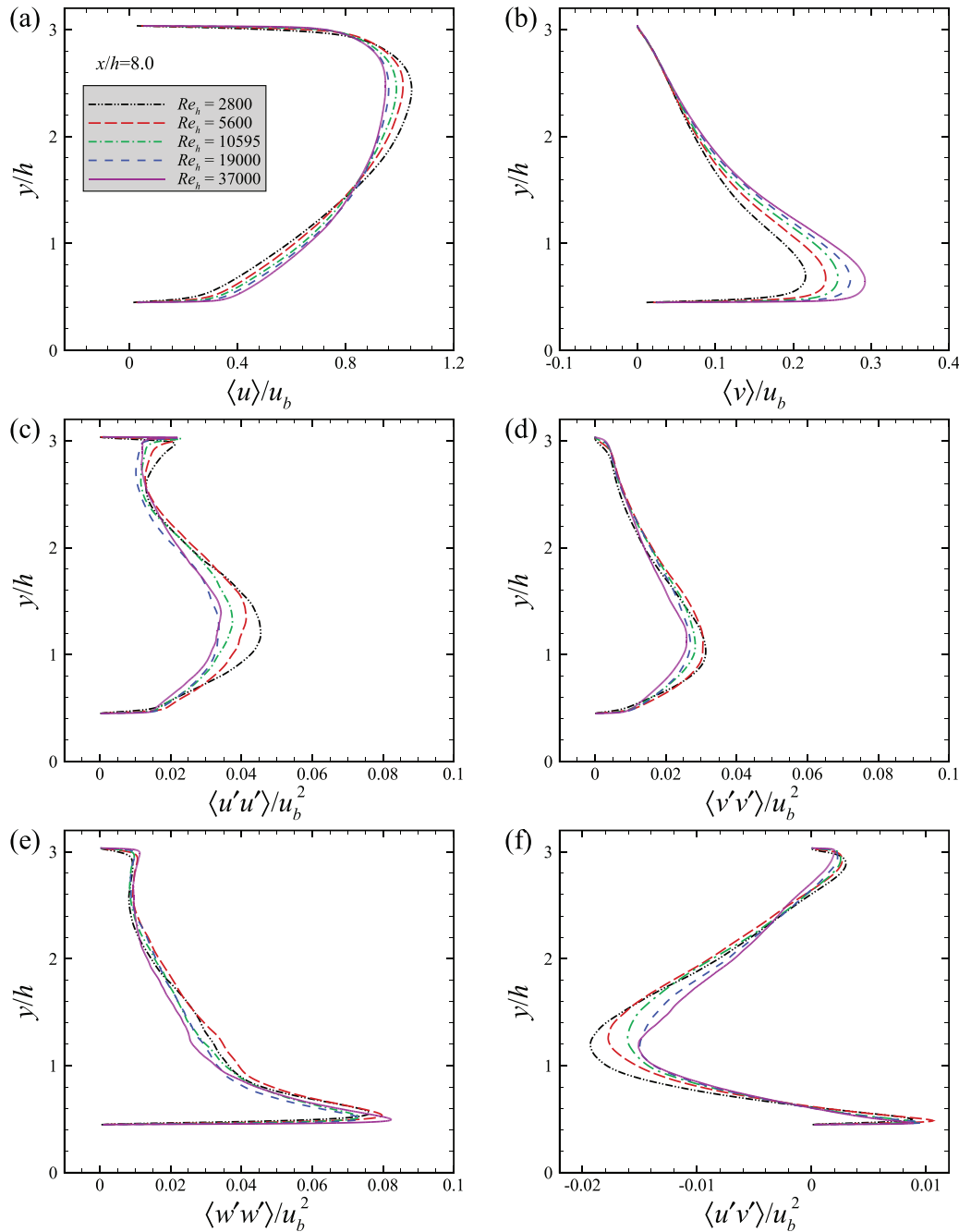
FIG. 12. Mean velocities (a and b) and Reynolds stresses (c–f) at $x/h = 8.0$.

skewness factors above and below the hill crest, respectively, suggesting higher probability of negative and positive vertical velocity fluctuations in the corresponding regions, respectively. With the increase in Reynolds number, the distribution of skewness becomes more fragmented due to the smaller turbulence

structures. For the flatness factors, the values computed from the streamwise velocity fluctuations, which are roughly larger than and smaller than three in upper and lower part of the region, respectively, are within the range of {2, 4} at most locations. The flatness factors of the vertical velocity fluctuations, on the other
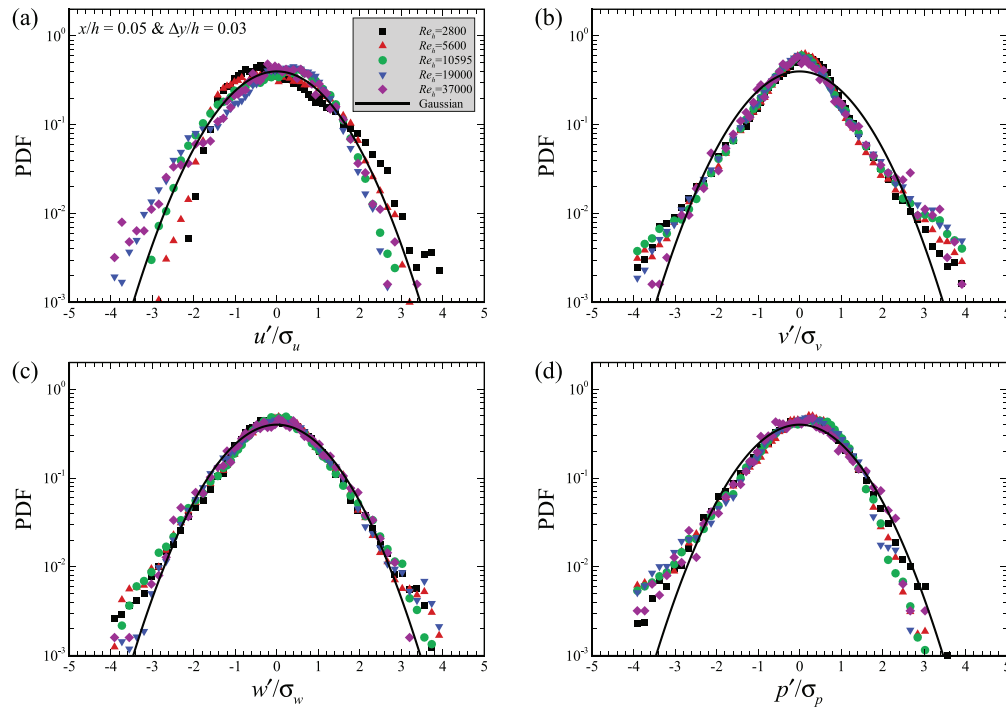
FIG. 13. PDFs of (a) streamwise, (b) vertical and (c) spanwise velocity fluctuations, and (d) pressure fluctuation at $\Delta y/h = 0.03$ vertically away from the bottom wall at $x/h = 0.05$.
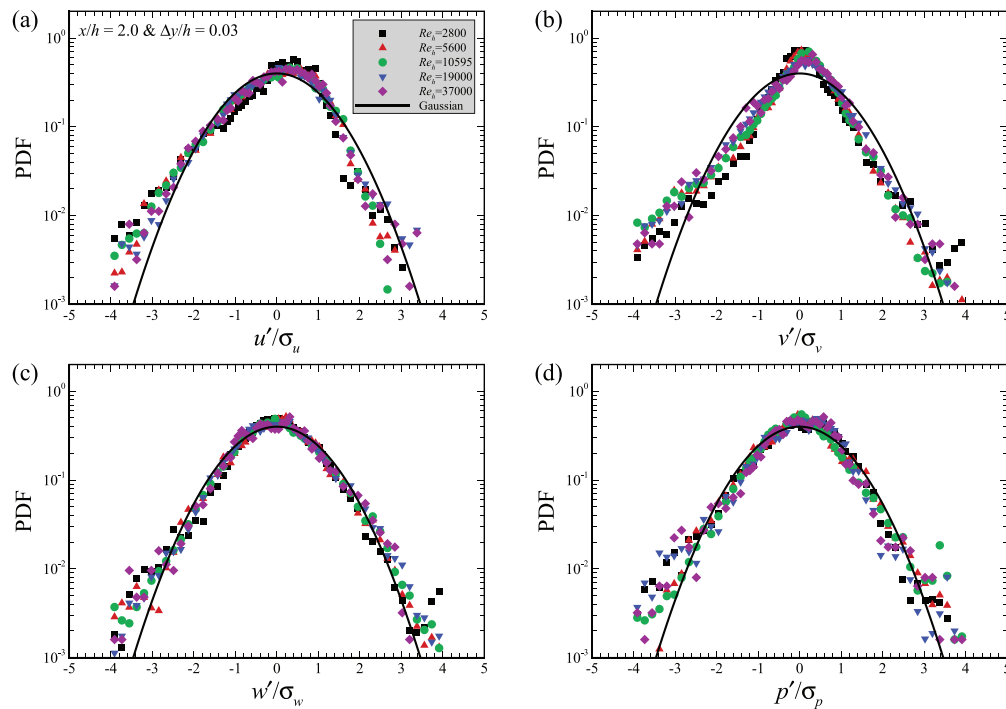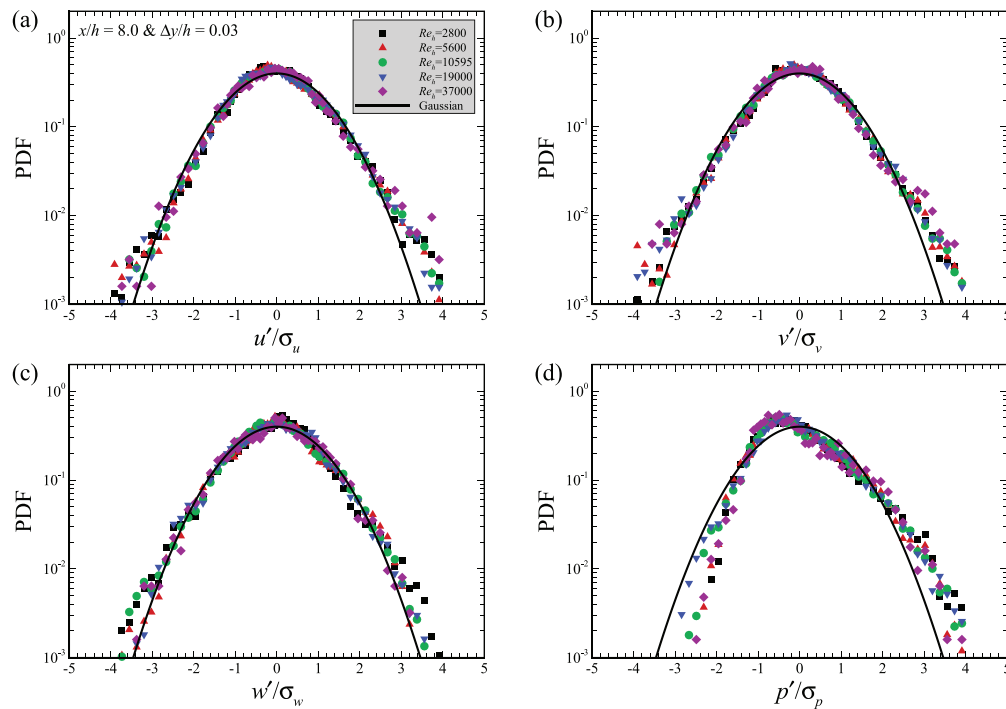

FIG. 14. PDFs of (a) streamwise, (b) vertical and (c) spanwise velocity fluctuations, and (d) pressure fluctuation at $\Delta y/h = 0.03$ vertically away from the bottom wall at $x/h = 2.0$.
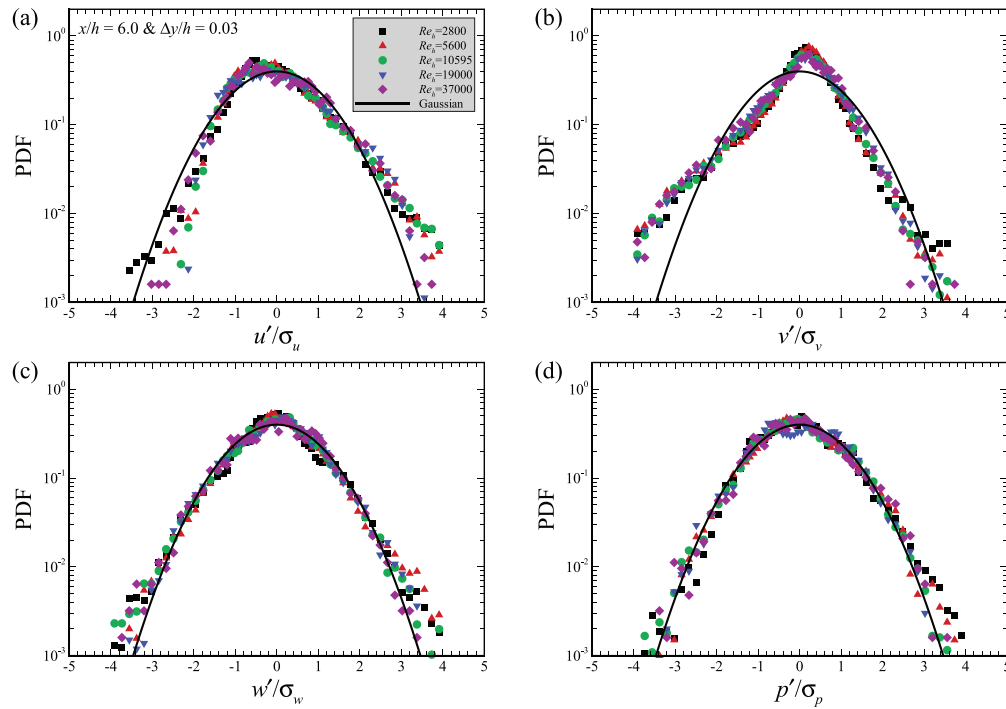
FIG. 15. PDFs of (a) streamwise, (b) vertical and (c) spanwise velocity fluctuations, and (d) pressure fluctuation at $\Delta y/h = 0.03$ vertically away from the bottom wall at $x/h = 6.0$.
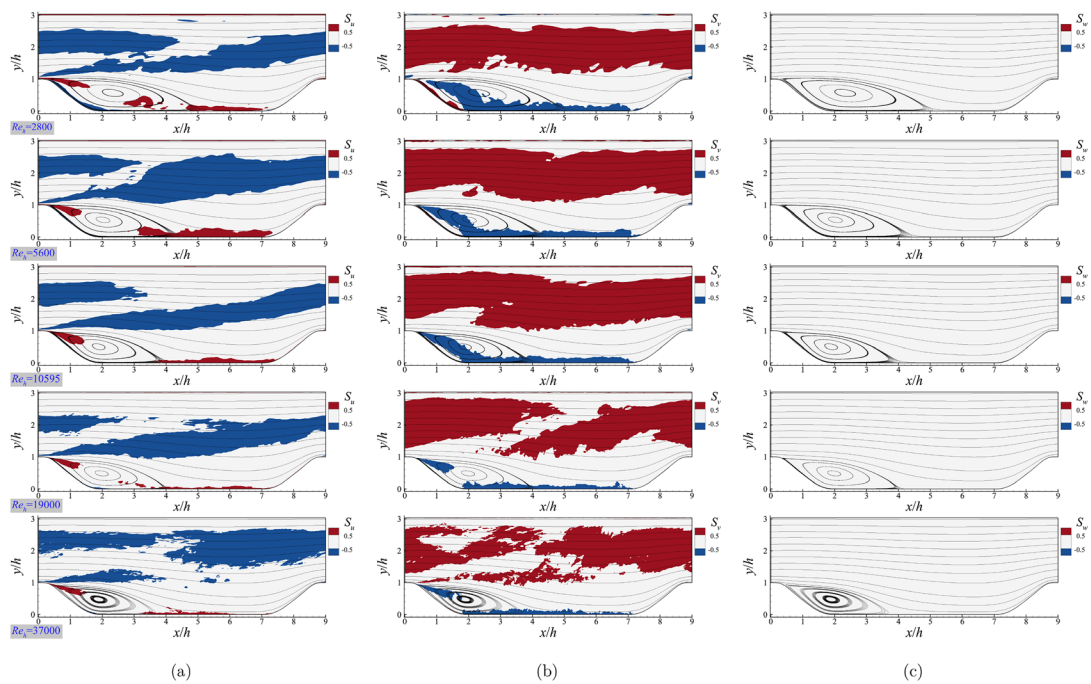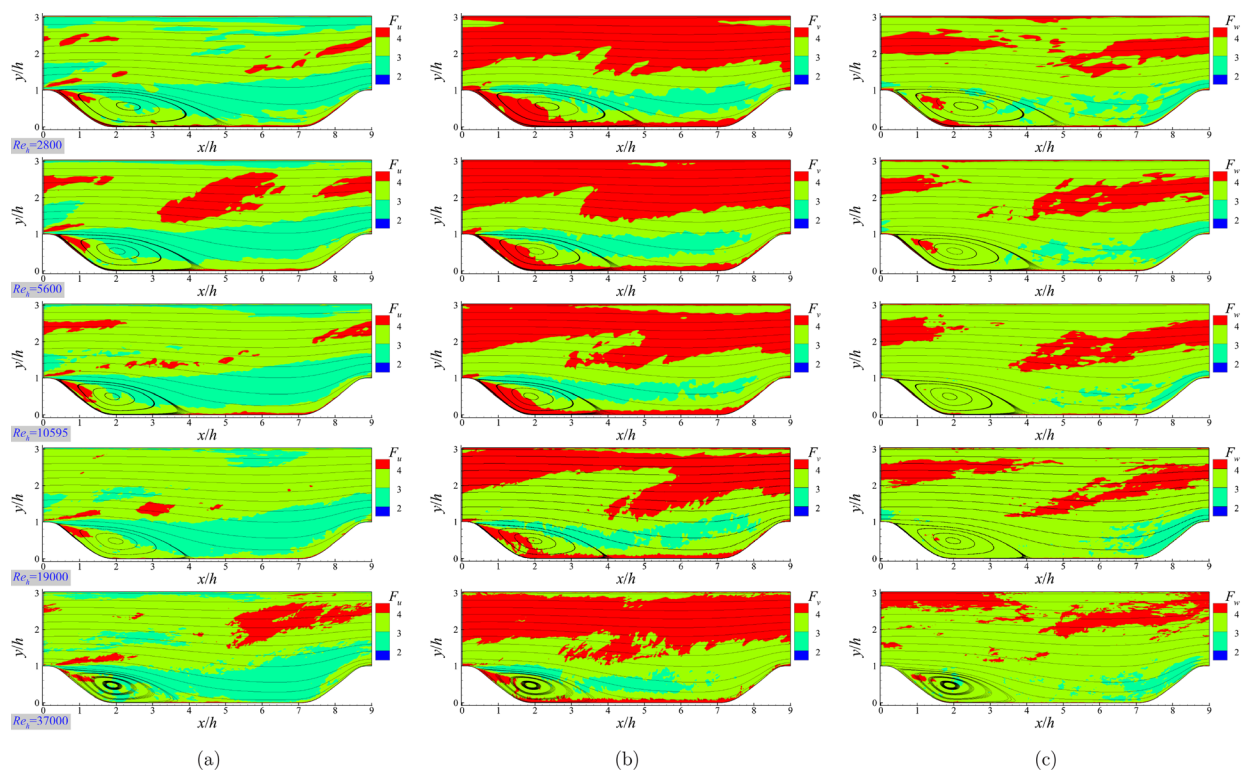

FIG. 16. PDFs of (a) streamwise, (b) vertical and (c) spanwise velocity fluctuations, and (d) pressure fluctuation at $\Delta y/h = 0.03$ vertically away from the bottom wall at $x/h = 8.0$.

FIG. 17. Contours of skewness factors of PDF for (a) streamwise, (b) vertical, and (c) spanwise velocity fluctuations for cases with $Re_h = 2800 - 37\,000$.

FIG. 18. Contours of flatness factors of PDF for (a) streamwise, (b) vertical, and (c) spanwise velocity fluctuations for cases with $Re_h = 2800 - 37\,000$.

hand, are equal to or larger than four in the upper part of the domain, which implies a higher probability of having velocity fluctuations of large magnitudes.

Figures 19 and 20 plot the joint PDFs of the streamwise and vertical velocity fluctuations at $\Delta y/h = 0.03$ and 1.0 on different vertical profiles, respectively.[46] First, the quadrant of scatter distribution indicates the sign of skewness factor, for example, the negative for streamwise velocity fluctuation and the positive for vertical velocity fluctuation at $\Delta y/h = 1.0$, and the range of scatter distribution indicates the magnitude of flatness factor, for example, larger for the streamwise and vertical velocity fluctuations at $\Delta y/h = 0.03$ and smaller at $\Delta y/h = 1.0$. Second, the wider scatter distribution at $\Delta y/h = 0.03$ demonstrates the possible existence of extreme events for the vertical velocity fluctuation. Finally and interestingly, the scatters mainly distributes at the first and third quadrants on the position of $x/h = 8.0$ and $\Delta y/h = 0.03$, which is responsible for the positive Reynolds shear stress. In addition, the Reynolds number effects can also be observed from the variation of scatter distribution ranges.

To quantify the decorrelation property of the flow quantities, we define the time correlation as

$$R_{xx} = \frac{\langle (x(t) - \langle x(t) \rangle)(x(t + \Delta t) - \langle x(t + \Delta t) \rangle) \rangle}{\sqrt{\langle (x(t) - \langle x(t) \rangle)^2 \rangle}\sqrt{\langle (x(t + \Delta t) - \langle x(t + \Delta t) \rangle)^2 \rangle}}, \quad (6)$$

where $\langle \rangle$ denotes the average over the flow domain and time, and Δt denote the time interval.

Similar to the aforementioned plots of PDF, Figs. 21–24 show the time correlations of velocity and pressure fluctuations at $\Delta y/h = 0.03$ in four vertical profiles. At $x/h = 0.05$, the time correlations of streamwise velocity fluctuation exhibit similar decaying tendency, but the deviations of curves between different Re_h increase with the increasing Δy. More importantly, the decay rate of time correlation increases monotonously with the Reynolds number for small temporal separations, which is mainly affected by the scale variations of turbulent structures in Fig. 8. For $x/h = 2.0 \sim 8.0$, the vertical distance $\Delta y/h = 0.03$ is located at the boundary layer for almost all the cases, and the case at higher Reynolds number exhibits the larger velocities and turbulent fluctuations. Thus, the monotonic variation of time correlation with Re_h can be seen for the four flow quantities, and it is most obvious for the vertical velocity fluctuation, which has the smallest decorrelation time shown by the display range at the horizontal axis. At $x/h = 2.0$, the time correlation of pressure
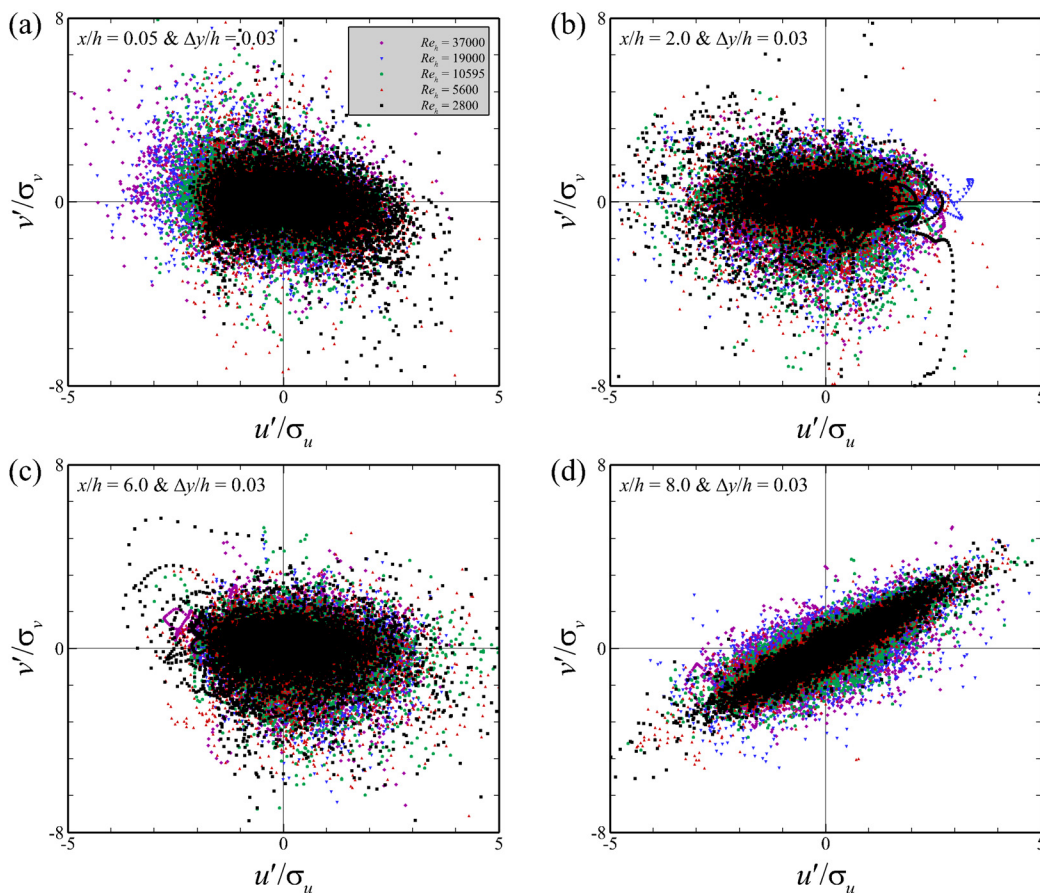
FIG. 19. Joint PDFs of the streamwise and vertical velocity fluctuations at $\Delta y/h = 0.03$ vertically away from the bottom wall at (a) $x/h = 0.05$, (b) $x/h = 2.0$, (c) $x/h = 6.0$, and (d) $x/h = 8.0$.
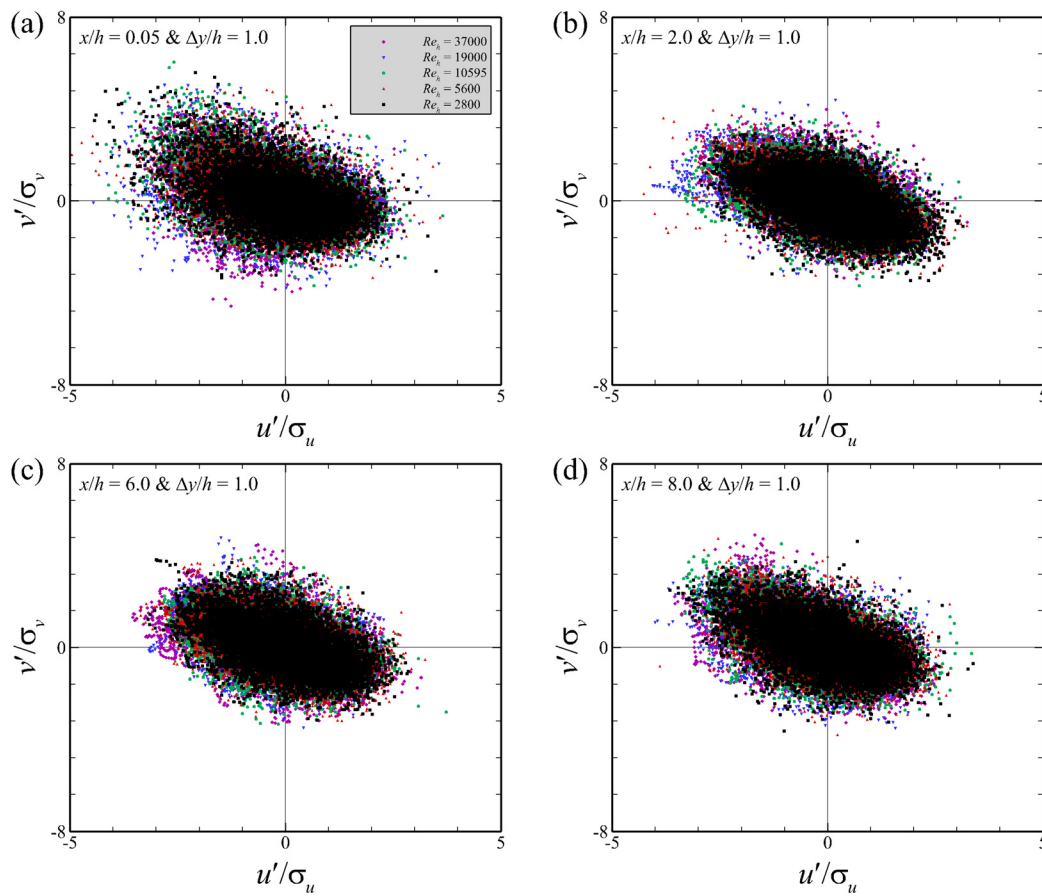
FIG. 20. Joint PDFs of the streamwise and vertical velocity fluctuations at $\Delta y/h = 1.0$ vertically away from the bottom wall at (a) $x/h = 0.05$, (b) $x/h = 2.0$, (c) $x/h = 6.0$, and (d) $x/h = 8.0$.

fluctuation exhibits a negative extreme value, demonstrating the existence of specific time scale. The time interval Δt reaching the extreme value increases with the decreasing Re_h, and the higher Δy, the smaller Δt (not shown in this paper, refer to Fig. 25).

After analyzing the time correlations at several specific locations, in this paper we examine the spatial distribution of the integral time scale on the x–y plane, which is defined as follows:

$$T = \int_0^\infty R(\tau)d\tau. \tag{7}$$

The computed integral time scales are shown in Fig. 25 for three components of velocity fluctuations at different Reynolds numbers. First, it is observed that the integral time scales of the streamwise velocity fluctuations are in general larger than the other two components. Regardless of the relative magnitudes, the time scales from both streamwise and vertical velocity fluctuations are larger in the recirculation zone when compared with the other region. For the integral scales of the spanwise velocity fluctuations, it is observed that they are larger in the layer next to the bottom wall and in the shear layer over the separation bubble. As for the comparison among integral time scales

computed from cases with different Reynolds numbers, the overall patterns are similar but with differences observed on certain local features like the location and the shape of the region with large integral time scales.

D. Reynolds number effects on characteristics of the recirculation zone

The separation bubble is the most important feature for the flow over periodic hills. In this section, we examine the characteristics of the separation bubble for different Reynolds numbers, which include the size and the center of the separation bubble, comparison of flow quantities, the budget of the mean kinetic energy on the coordinate with its center fixed at the bubble center, and the power spectral density of velocity fluctuations at two locations within the separation bubble and in the shear layer, respectively.

First, we examine the size and the center of the separation bubble. As illustrated in Fig. 3, the center of the recirculation zone is identified as the location with zero mean streamwise and vertical velocities. The obtained coordinates of the recirculation center from cases with
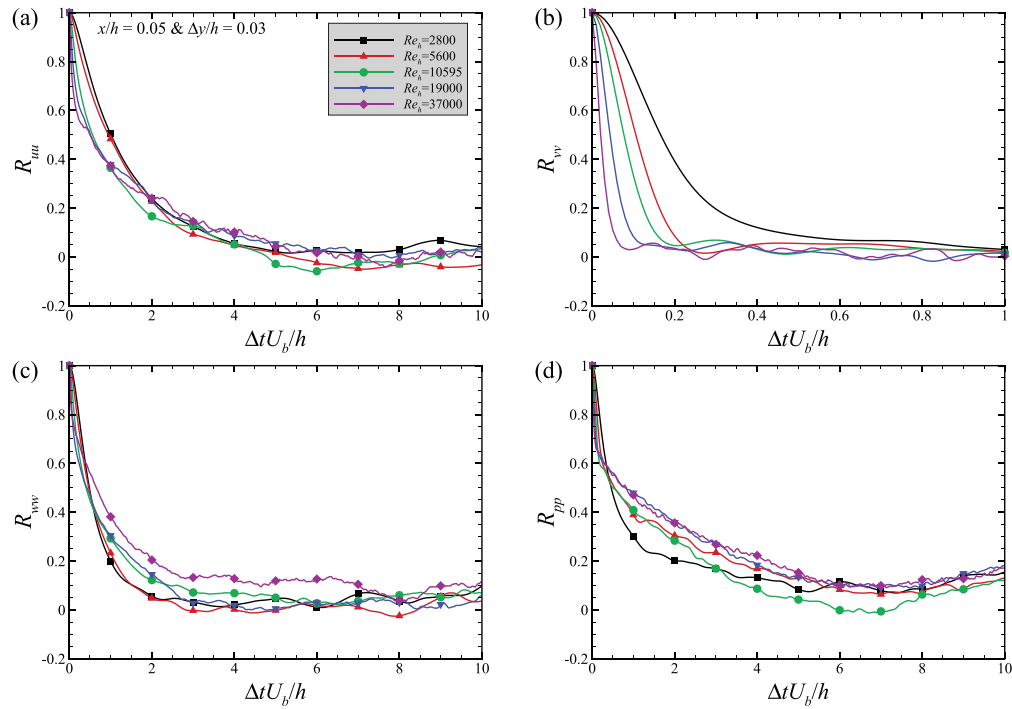
FIG. 21. Time correlations of (a) streamwise, (b) vertical and (c) spanwise velocity fluctuations, and (d) pressure fluctuation at $\Delta y/h = 0.03$ vertically away from the bottom wall at $x/h = 0.05$.
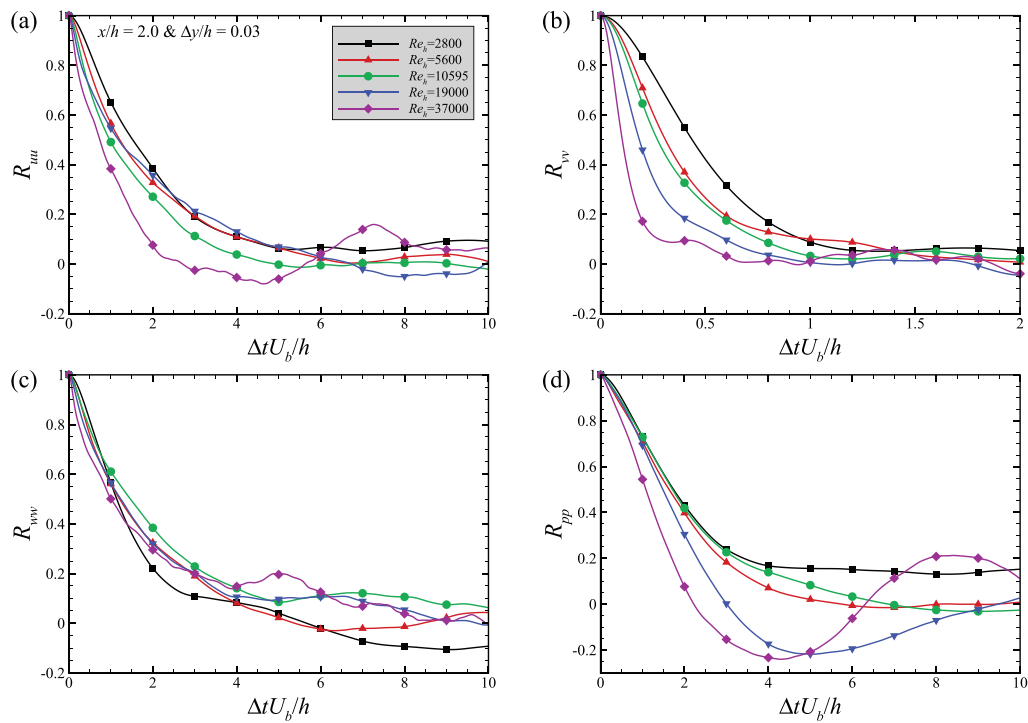
FIG. 22. Time correlations of (a) streamwise, (b) vertical and (c) spanwise velocity fluctuations, and (d) pressure fluctuation at $\Delta y/h = 0.03$ vertically away from the bottom wall at $x/h = 2.0$.

different Reynolds numbers are shown in Fig. 26. As seen, the vertical center of the separation bubble moves downward with increasing Re_h, demonstrating the flattening effect of increasing Reynolds number on the height of the separation bubble. The streamwise location of the separation bubble is observed moving upstream with the increase in Re_h, being consistent with the upstream movement of the reattachment point as shown in Fig. 7. A local minimum for the streamwise coordinate of the bubble center appears at $Re_h = 10\,595$. Moreover, it is observed that the differences between the streamwise locations of the separation bubble at $Re_h = 10\,595$, $19\,000$, and $37\,000$ are less than 5%.

We have shown the separation and reattachment points, the center of the separation bubble in Figs. 7 and 26, respectively. To get a better idea on the changing of the bubble geometry with Re numbers, the streamlines enclosing the separation bubble with its center are shown in Fig. 27. As seen, the bubble shrinks in size mostly in its rear part as the Reynolds number increases, with significant differences on the reattachment points, while less changes on the center of the separation bubble, especially for Reynolds number higher than 2800.

Figures 28 and 29 plot the mean velocities and Reynolds stresses on the vertical and horizontal lines passing through the center of the recirculation zone as demonstrated in Fig. 3. As seen, on the coordinate with its origin located on the center of the recirculation zone, the overall variations in the vertical and streamwise directions are similar with each other. First, we examine the flow characteristics along the vertical line passing through the bubble center. It is observed from Fig.

28(a) that the mean streamwise velocity from different Reynolds numbers overlaps with each other in the separation bubble except in the near wall region because of the different distances of the bubble center from the wall. For the mean vertical velocity, upward and downward motion is observed in the lower part and upper part of the bubble, with the magnitude of the downward velocity increasing with the increase in Reynolds number by approximately 25% for Re_h changing from 2800 to 37 000. The upward motion is also observed on the vertical line but without observing an asymptotic behavior. For different components of the Reynolds stresses, similarities are observed for the overall variations in the vertical directions. Differences, on the other hand, are observed on their magnitudes with the maximum differences approximately 20%. The peaks of the magnitudes of the Reynolds stresses are observed located around the top boundary of the separation bubble. The maximum values of $\langle u'u' \rangle$ are observed larger than the other two components with similar magnitudes. One interesting observation is that $\langle u'u' \rangle$, $\langle v'v' \rangle$, $\langle w'w' \rangle$ and $\langle u'v' \rangle$ all vary in almost a linear way except for $\langle w'w' \rangle$ in the very near wall region for high Reynolds numbers, where peaks are observed. Overall, similarities are in general observed on the vertical line passing through the bubble center.

Then, we examine the flow characteristics along the horizontal line passing through the bubble center. In Fig. 29(a) for the streamwise velocity, differences are observed at locations both upstream and downstream of the bubble center probably because of the change of bubble length in both directions. At locations downstream of the
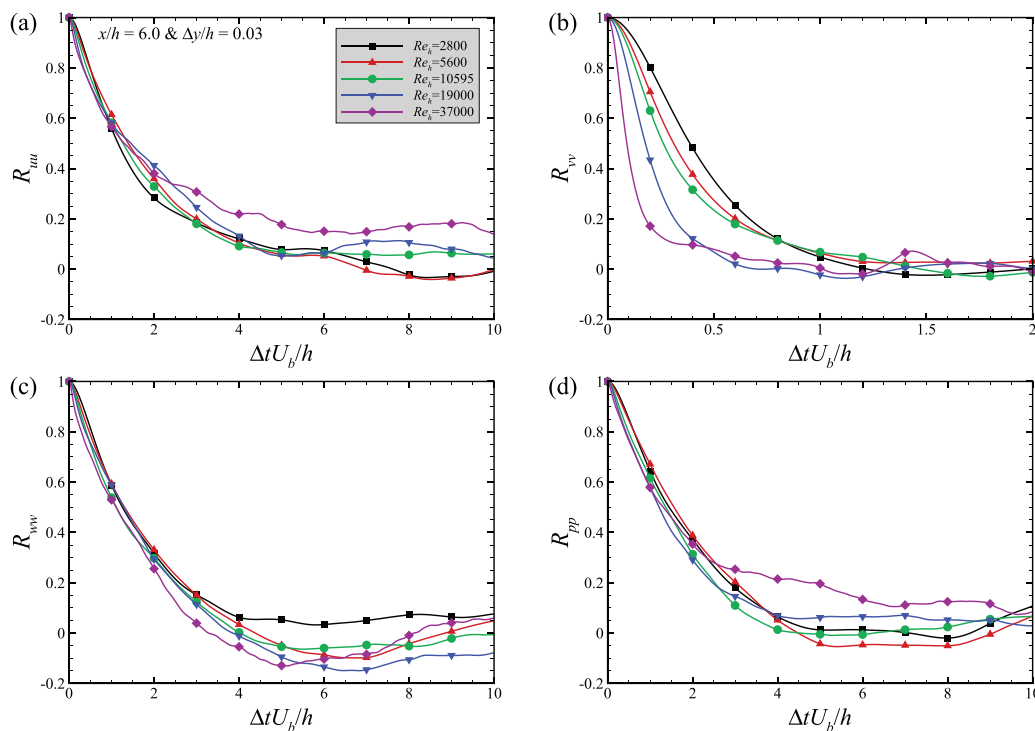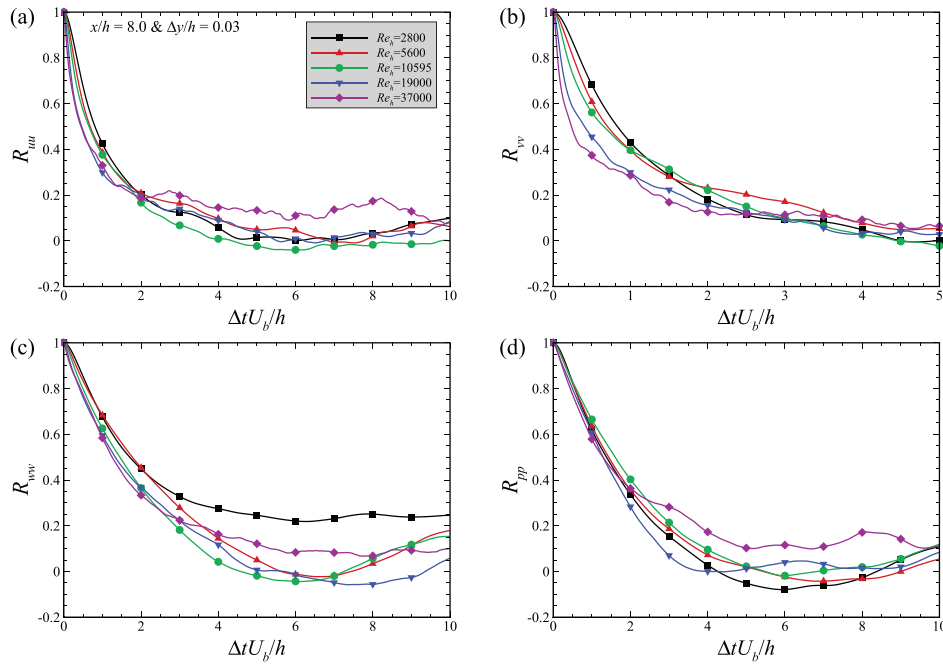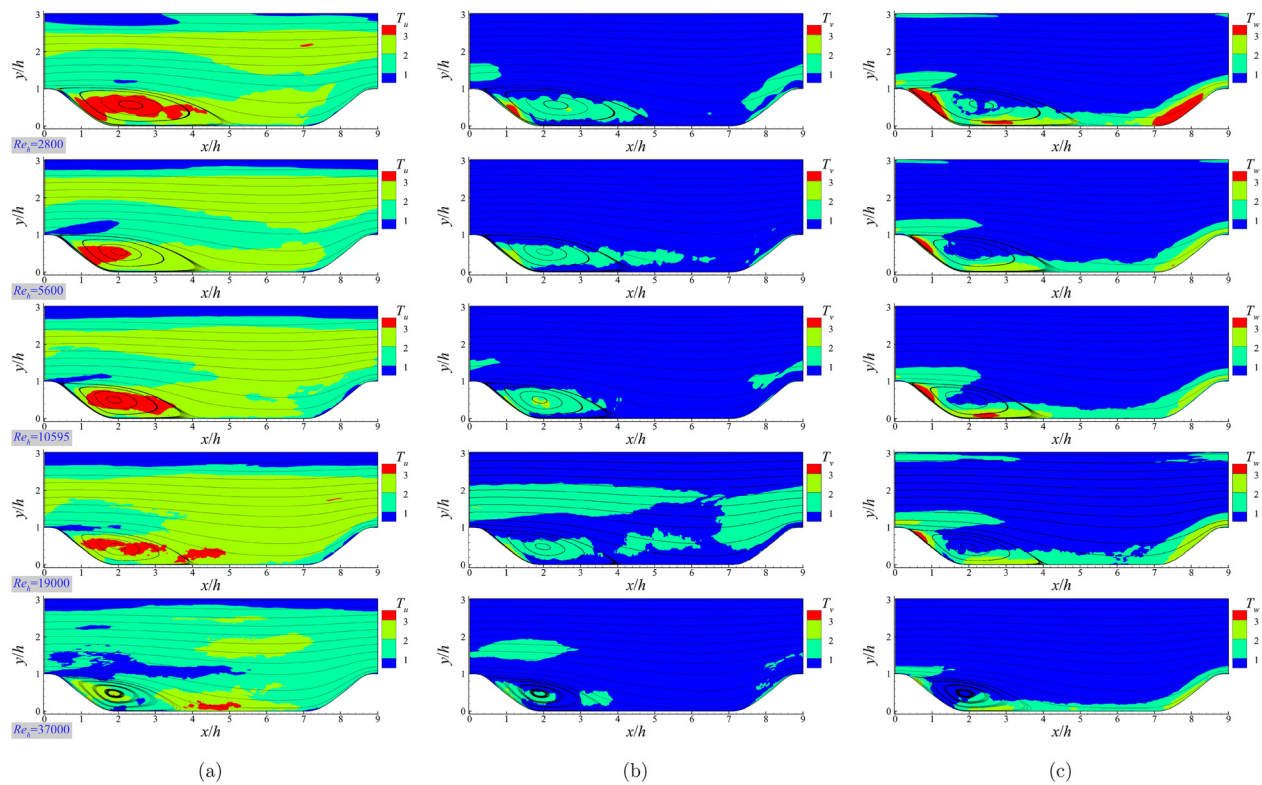

FIG. 23. Time correlations of (a) streamwise, (b) vertical and (c) spanwise velocity fluctuations, and (d) pressure fluctuation at $\Delta y/h = 0.03$ vertically away from the bottom wall at $x/h = 6.0$.

FIG. 24. Time correlations of (a) streamwise, (b) vertical and (c) spanwise velocity fluctuations, and (d) pressure fluctuation at $\Delta y/h = 0.03$ vertically away from the bottom wall at $x/h = 8.0$.

FIG. 25. Contours of integral time scale for (a) streamwise, (b) vertical, and (c) spanwise velocity fluctuations for cases with $Re_h = 2800$–$37\,000$.
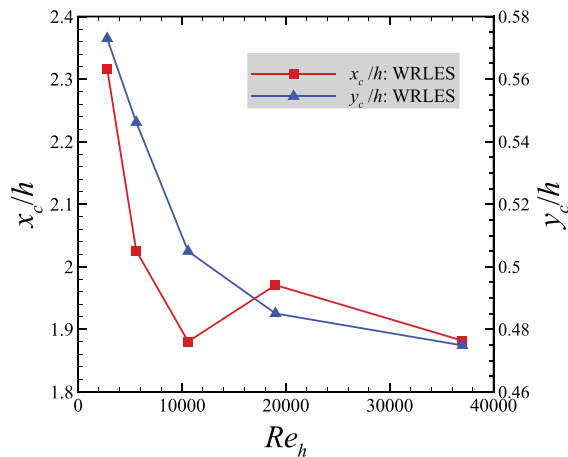
FIG. 26. The streamwise and vertical coordinates of the center of the recirculation zone at different Reynolds numbers.

bubble center, the magnitude of the streamwise velocity increases monotonically with the increase in Reynolds number by approximately 20% at $3h$ from the center. As for the vertical velocity shown in Fig. 29(b), its maximum magnitude upstream of the bubble center is increased by as high as 40% when Re_h changed from 2800 to 5600 and higher. At locations downstream of the bubble center, on the other hand, no significant differences are observed. Together with Figs. 28(a) and 28(b), it shows that the velocity magnitude in the upper region of the bubble increases monotonically with the increase in the Reynolds number, while that in the lower part of the separation bubble does not change obliviously with the Reynolds number. For the streamwise variations of the Reynolds stresses shown in Figs. 29(c)–29(f), surprisingly it is observed that the overall variations are similar with each other for different Reynolds numbers, even though the bubble lengths change by approximately $1.5h$. Unlike the variations close to linear observed in the separation bubble in the vertical direction, a peak at approximately h from the bubble center is observed for all the considered Reynolds numbers. As for the magnitudes of Reynolds stresses, differences less than 20% are observed for different Reynolds numbers. Together with the observations on the vertical line, similarities are in general observed for the mean velocity and Reynolds stresses, except for the mean velocity in the upper part of the separation bubble where
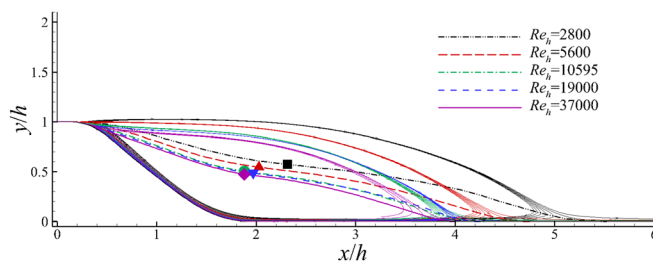

FIG. 27. The range of recirculation zone represented by the streamlines at various Reynolds numbers. The symbols denote the center of the recirculation zone, and the thick lines denote the isolines of zero mean streamwise velocity, which divide the recirculation zone into two parts.

asymptotic behavior is observed. This indicates that the bulk velocity (U_b) and the hill height (h) are appropriate for characterizing these large-scale structures.

So far, similarities are in general observed for the flow characteristics within the separation bubble. However, we have observed the significant changes of the geometry of the separation bubble, especially its length. To find the causes for these phenomena, we examine different terms in the budget equation for MKE, which is formulated as

$$0 = -\langle u_j \rangle \frac{\partial \langle u_i \rangle \langle u_i \rangle / 2}{\partial x_j} - \frac{\partial}{\partial x_j} \left(\frac{1}{\rho} \langle p \rangle \langle u_j \rangle + \langle u_i' u_j' \rangle \langle u_i \rangle \right.$$
$$\left. - 2(\nu + \nu_t) S_{ij} \langle u_i \rangle \right) + \langle u_i' u_j' \rangle \frac{\partial \langle u_i \rangle}{\partial x_j} - 2(\nu + \nu_t) S_{ij} \frac{\partial \langle u_i \rangle}{\partial x_j}, \quad (8)$$

where the various terms of the right-hand side of the above equation are in the order: (1) the convection of the MKE by the mean flow (MC, mean convection); (2) transport terms due to mean pressure (PT, pressure transport), turbulence fluctuations (TC, turbulence convection), and diffusion due to molecular and eddy viscosity (DF); (3) loss in MKE (negative production) due to transfer of energy from the mean flow to turbulence (TP, turbulence production); and (4) dissipation (DP).

Figures 30 and 31 show the vertical profiles of MKE budget at different streamwise locations relative to the bubble center to investigate how the mean kinetic energy is transported downward for different Reynolds numbers. First, it is observed that different terms in the MKE budget equation vertically vary in a similar way at different streamwise locations. The key contributing terms are the MC, TC, PT, and TP terms, while the magnitudes of the DF and DP terms are relatively small, which will not be discussed in detail. Different terms play different roles. MC term in general plays as a source of MKE at different locations, while the PT and TP terms in general extract energy from the MKE. The role of the TC term is complicated that it is mostly negative above the top boundary of the separation bubble, while it is positive in the separation bubble, indicating that it plays an important role in advecting the MKE from the shear layer and above downward into the separation bubble. The MKE within the shear layer and above, on the other hand, is mainly brought into via the MC term. Below the top boundary of the separation bubble, the MC term, which is balanced by the TP and TC terms, plays a role in extracting energy from the MKE for locations upstream the center of the bubble, while these are negligible downstream the center of the separation bubble. Although the PT term extracts energy from MKE at most locations, it adds energy to MKE around the shear layer at $1\,h$ and $0.5h$ upstream of the bubble center, and below the bubble center at locations downstream of the bubble center, respectively, which can be related to the adverse pressure gradient for $x/h \in [2.2, 4.0]$ as shown in Fig. 6(c) and the variation of mean streamwise velocity. In the very near wall region at locations downstream of the bubble center, negative values of the MC and TC terms and positive value of TP term are observed in Fig. 31, which is probably related to the negative wall shear stress.

Comparing different terms at different streamwise locations, it is observed that the maximum of the MC term is largest at $1.5h$ upstream of the bubble center, decrease abruptly until $0.5h$ upstream of the bubble center, remains nearly the same (slightly increase from the bubble center to its $0.5h$ downstream) at further downstream locations. Similar downstream variations are observed for the maximum
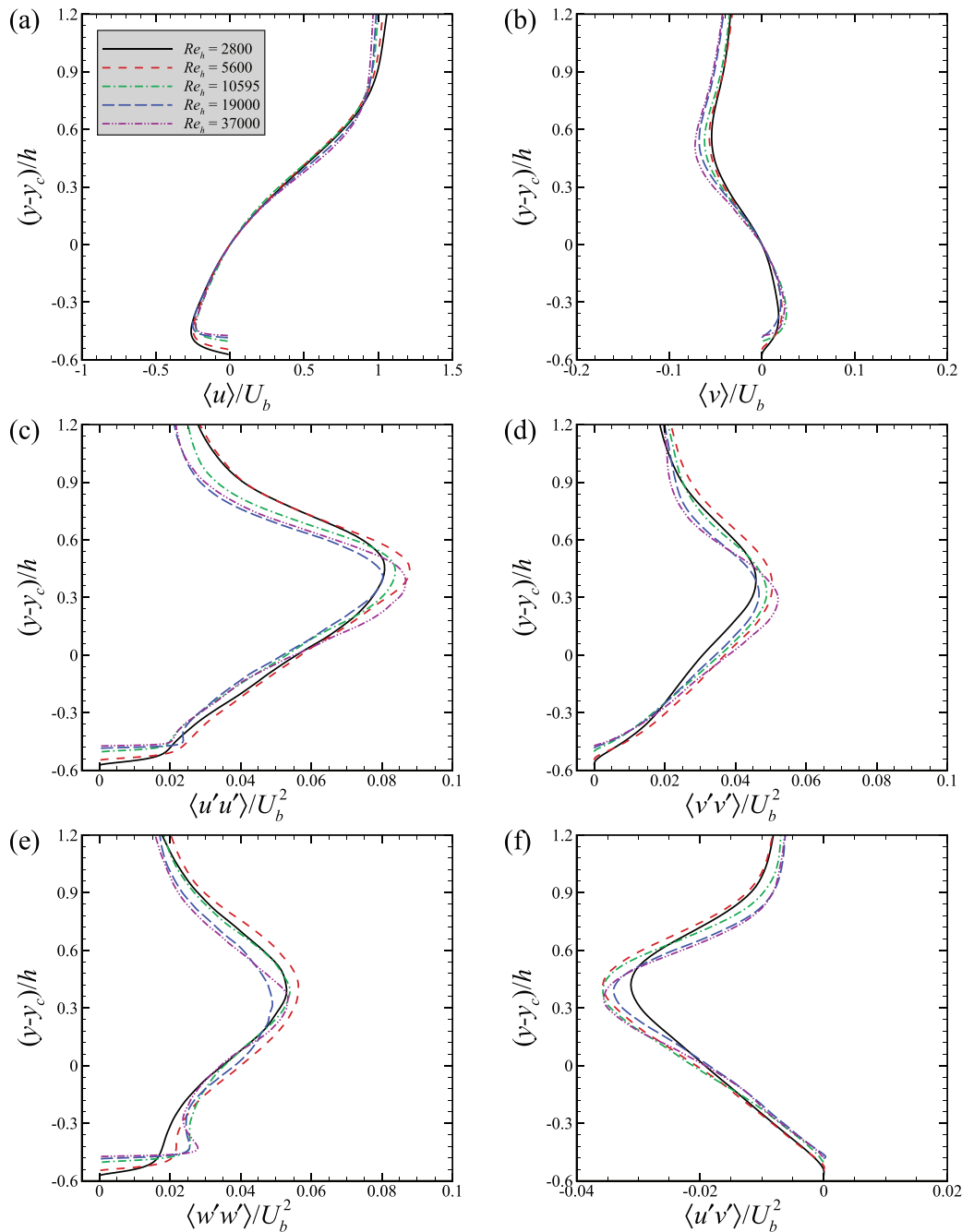
FIG. 28. Mean velocities (a and b) and Reynolds stresses (c–f) at the $z-$ profile through the center of the recirculation zone.

of the TC term. For the PT term, relatively complex vertical variations are observed at locations upstream of the bubble center. After the bubble center, the maximum magnitudes of the PT term gradually increase as moving further downstream. For the TP term, the maximum magnitude is also observed at $1.5h$ upstream of the bubble

center, abruptly decrease until $0.5h$ bubble upstream, and gradually decrease at further downstream locations. One interesting observation is that the location for the peak of the MC term is located approximately 0.5–$0.7h$ above the bubble center for all downstream locations, although the height of the separation bubble gradually decreases as
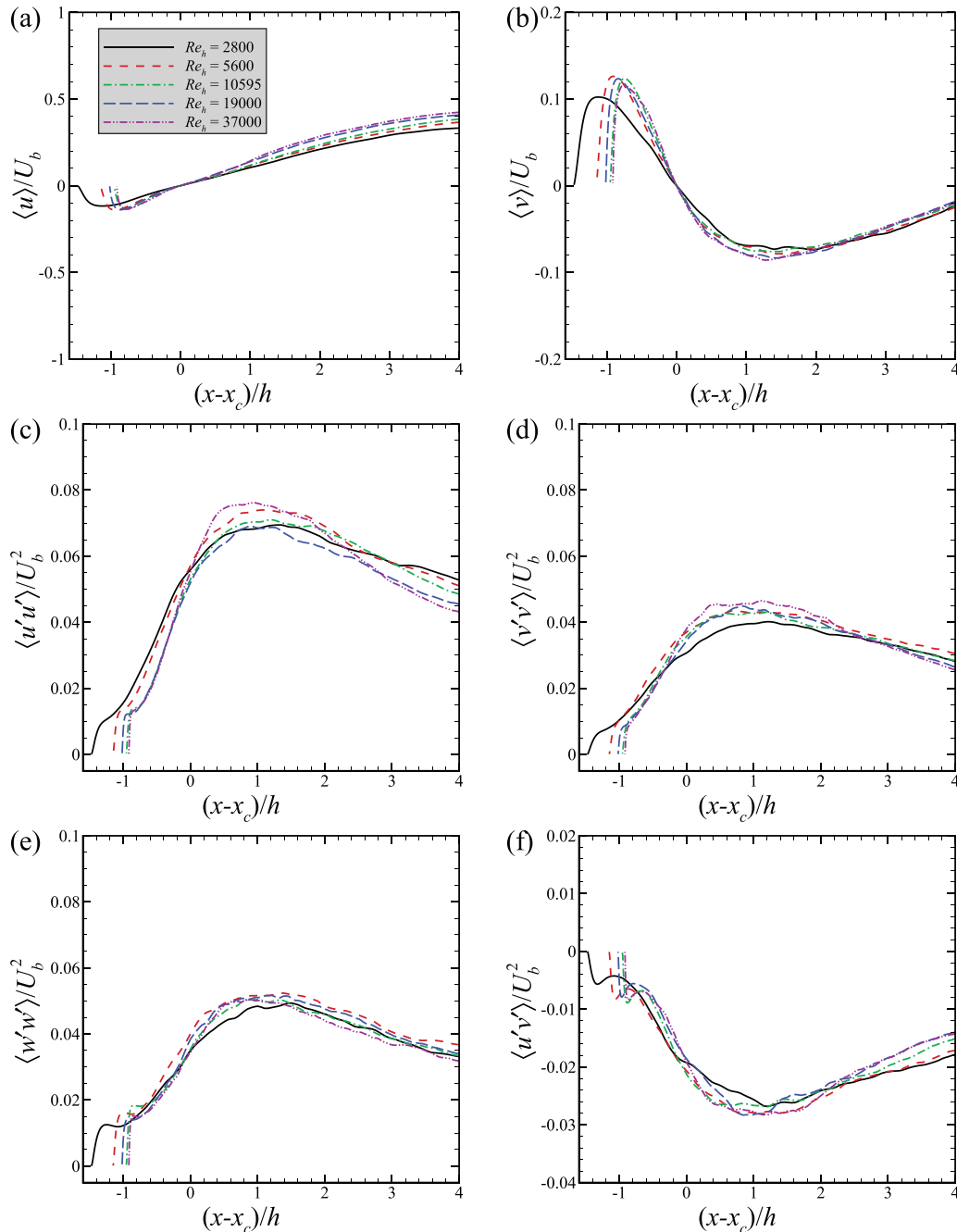
FIG. 29. Mean velocities (a and b) and Reynolds stresses (c–f) at the $y-$ profile through the center of the recirculation zone.

traveling downstream. For the vertical location of the maximum of the TC term, it gradually decreases from approximately $0.5h$ above the center at $x_c - 1.5h$ to $0.15h$ at $x_c + 1.5h$. The vertical location for the peak of the TP term is also observed decreasing as moving downstream from approximately $0.5h$ above the bubble center at $x_c - 1.5h$ to $0.3h$ at $x_c + 1.5h$.

As for the comparison between different Reynolds numbers, significant differences are observed upstream the center of the separation bubble, especially at $x_c - 1.5h$ and $x_c - 1h$ locations. It is observed that the higher the Reynolds number, the higher the maxima of the MC and TC terms, especially at $x_c - 1.5h$. Another interesting phenomena observed at $x_c - 1.5h$ is that the maximum of the TC term
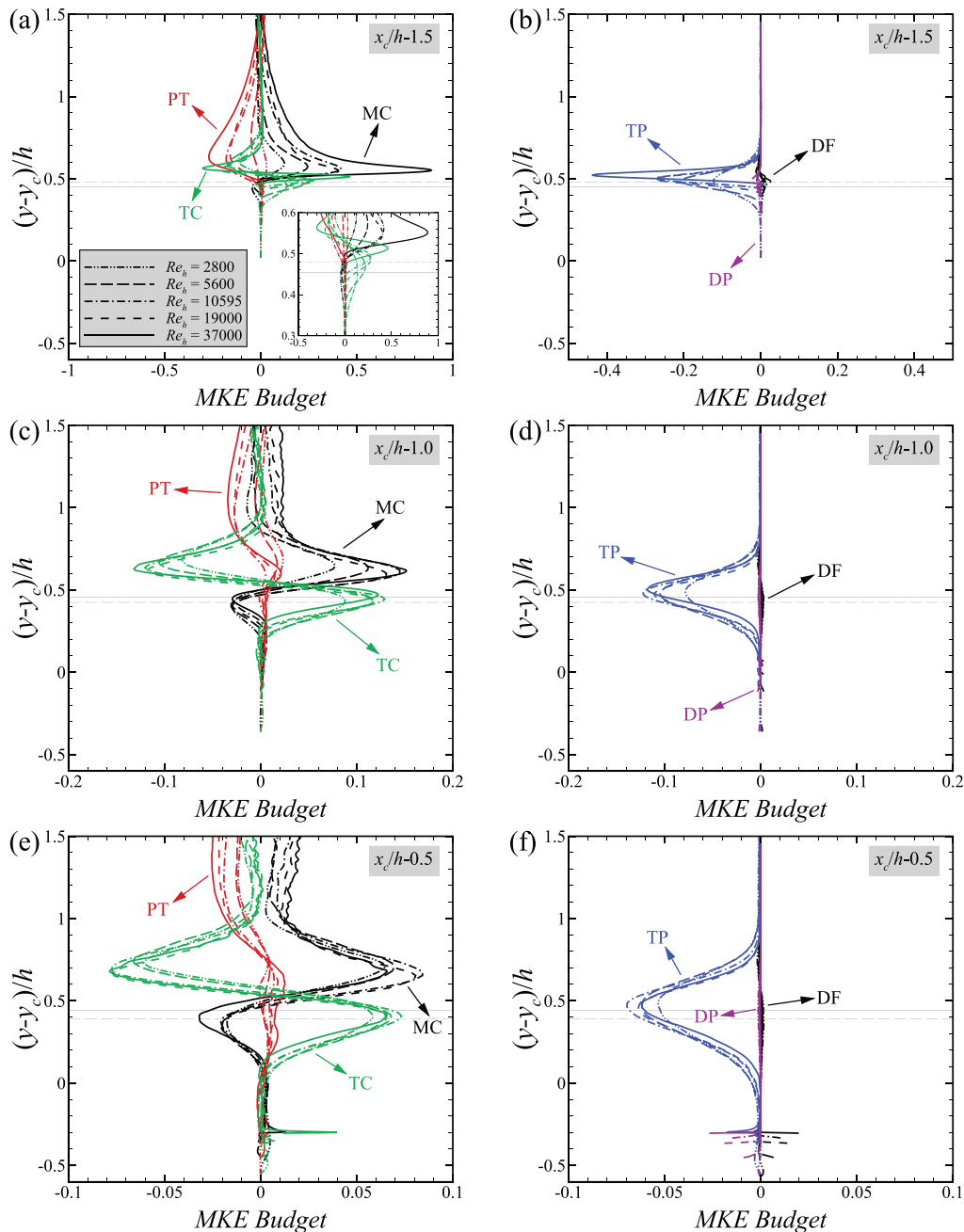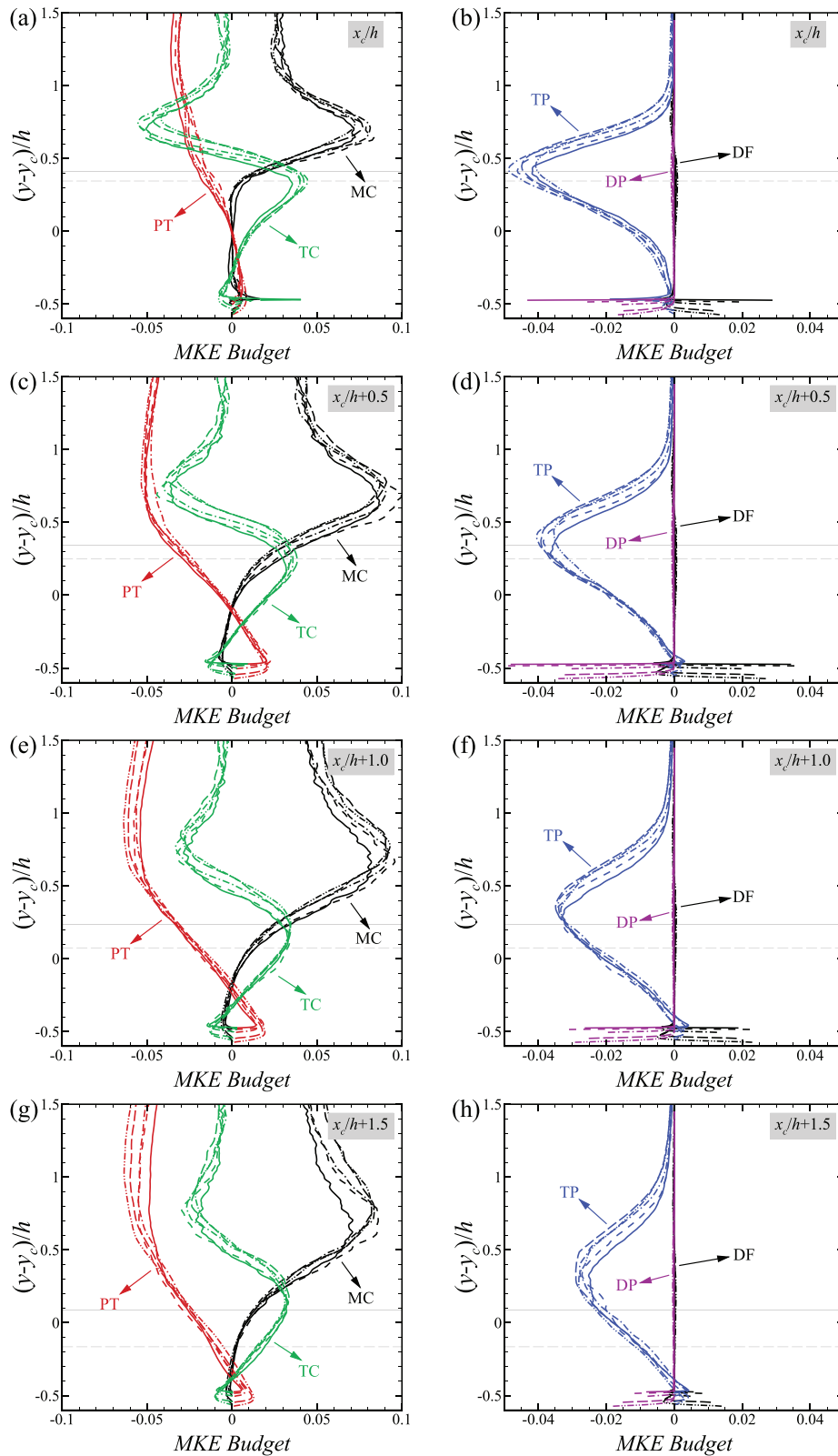
FIG. 30. Vertical profiles of MKE budget for different Reynolds numbers at (a and b) 0.5h, (c and d) 1.0h, and (e and f) 1.5h upstream of the recirculation center. The gray solid line and long-dashed line denote the upper edge of recirculation zone at $Re_h = 2800$ and 37 000, respectively.

moves upward with the region with positive TC term becoming narrower with the increase in the Reynolds number, indicating the role of smaller eddies in advecting MKE at higher Reynolds numbers. At locations downstream of the bubble center, the vertical variations (including locations of peaks and magnitudes) are similar for different Reynolds numbers with the maximum differences approximately 20%.

Overall, these results suggest that the smaller separation bubble observed at higher Reynolds number is caused by the higher mean convection (related to the thinner boundary layer) and increased turbulence convection at higher Re numbers.

To examine the frequency characteristics in the recirculation zone and in the shear layer above, the power spectral density (PSD) of

FIG. 31. Vertical profiles of MKE budget for different Reynolds numbers at (a and b) the recirculation center, (c and d) 0.5h, (e and f) 1.0h, and (g and h) 1.5h downstream of the recirculation center.
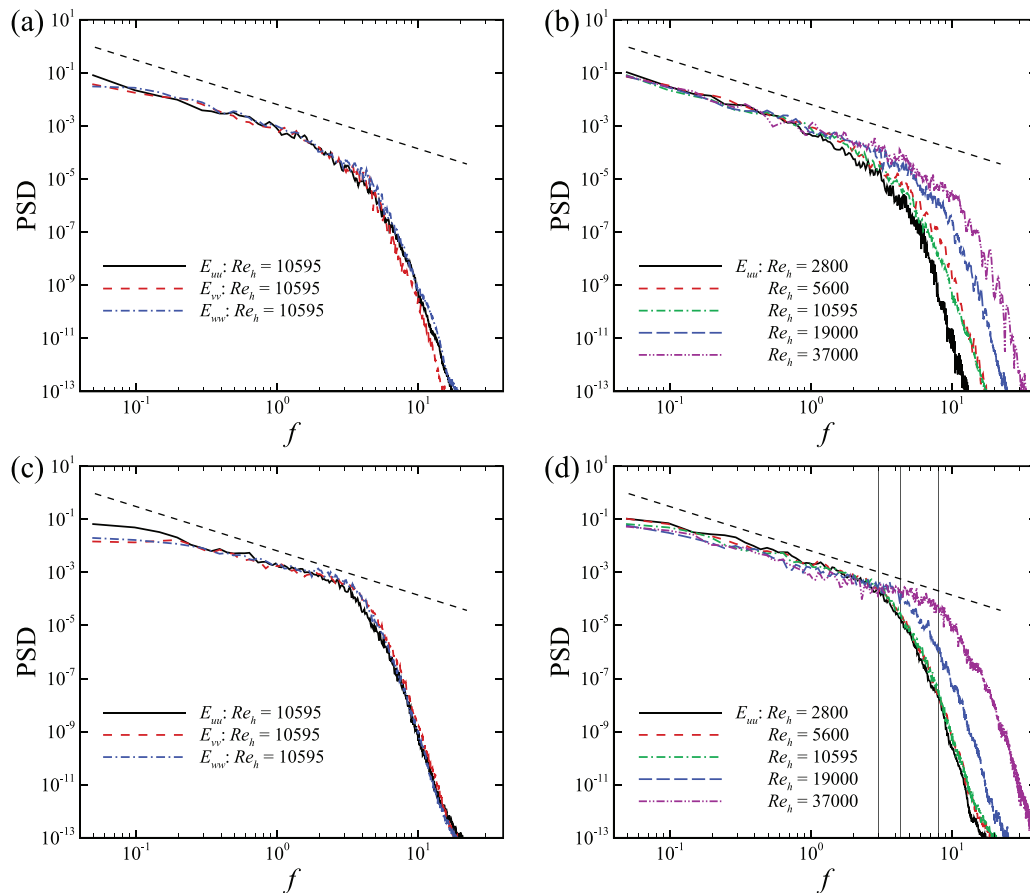
FIG. 32. Power spectral density of one-dimensional spectra of (a and c) the three velocity components and (b and d) the streamwise component at different Reynolds numbers. The results for the center of the recirculation zone and the location in the shear layer at $x/h = 2.23$, $y/h = 1.13$ are shown in subfigure (a and b) and (c and d), respectively.

the velocity fluctuations in time at two typical points (shown in Fig. 3) is calculated and compared in Fig. 32. First, it is observed that at both points, a range of the spectra follows a slope close to $-5/3$, which indicates the existence of the inertial subrange, for all the velocity components and all considered Reynolds numbers. The cutoff frequency for the inertial subrange increases monotonously with the Reynolds number for the point located within the bubble. For the point located in the shear layer, on the other hand, the critical frequency is the same for the three lower Reynolds numbers and then increases monotonously for higher Reynolds numbers. Comparing the PSD at the two points, it is seen that the PSD of the three components is close to each other at the point located within the separation bubble, while in the shear layer the PSD of the streamwise velocity fluctuations is higher than the other two components at low frequencies, indicating the turbulence within the bubble are more isotropic compared with that in the shear layer. As for the critical frequency, its value is observed higher (i.e., wider inertial range) within the shear layer when compared with that in the separation bubble, revealing higher local Reynolds number and richer turbulence structures within the shear layer.

V. CONCLUSION

WRLES of flow over periodic hills are carried out for studying the Reynolds number effect on the flow statistics. Five different Reynolds numbers ranging from 2800 to 37 000 are considered. To validate the accuracy of the present simulations, the vertical profiles of the mean velocities and Reynolds stresses are detailedly compared with the DNS, WRLES, and experimental data in the literature.

The dependence of global flow features on Reynolds number is examined by comparing the skin friction and pressure coefficients from different cases. The comparison shows that the magnitude of friction coefficient in general decreases with the increase in Reynolds number, while the pressure coefficient varies in the opposite direction. For the largest two Reynolds numbers (i.e., $Re_h = 19\,000$, 37 000), differences between the friction coefficients are still observed, while the pressure coefficients almost overlap with each other. As for the instantaneous flow structures identified using the isosurfaces of pressure fluctuation and Q criteria, it is observed that the higher the Reynolds number, the smaller the turbulence structures. The vertical profiles of the time-averaged flow statistics at four typical streamwise locations are examined in detail. It is shown that the mean streamwise velocity

exhibits monotonous variations with the Reynolds number at all four streamwise locations, with the negligible differences between the predictions from $Re_h = 19\,000$ and $37\,000$. For the vertical profiles of the vertical component of the mean velocity and the Reynolds stresses, asymptotic behavior is observed at locations without flow separations, which is less pronounced at the location (i.e., $x/h = 2$) featured by the separation bubble.

Then, the statistical properties of turbulence structures are examined via the PDF and the time correlation of velocity fluctuations. The results show that the PDF of the spanwise velocity fluctuation can be approximated well with the Gaussian distribution, while those of the streamwise and vertical velocity fluctuations deviate at different extents from the Gaussian distribution at different locations. An overall similar pattern of the skewness and flatness factors of the PDFs is observed for cases with different Reynolds numbers. For the time correlation, the decay rate increases monotonously with the Reynolds number for small temporal separations, which is due to the smaller turbulence structures observed at higher Reynolds number. For the integral time scale, an overall similar distribution is observed for cases with different Reynolds numbers with those of the streamwise velocity fluctuation larger than the other two components.

At last, the dynamics and the Reynolds number effects are investigated for the separation bubble, which is the most important feature for the flow over periodic hills, by analyzing the flow statistics, the MKE budget on the coordinate with its origin fixed at the center of the separation bubble, and the power spectral density of velocity fluctuations from a point in the bubble and a point in the shear layer. For the geometrical features of the separation bubble, it is observed that with the increase in Reynolds number it shrinks in size both vertically and horizontally mostly in the rear part. For the comparison of mean velocities and Reynolds stresses on the coordinate with its origin located on the recirculation center, similarities are in general observed for different Reynolds numbers except for the mean velocity in the upper part of the separation bubble where asymptotic behavior is observed. To further probe into the dynamics of the separation bubble, we examine different terms in the budget equation for mean kinetic energy and the power spectral density of velocity fluctuations in the separation bubble and in the shear layer, respectively. As for the power spectral density, a wider inertial subrange is observed for higher Reynolds numbers. The results of the MKE budget show that the mean convection (MC) term and the turbulence convection (TC) term play an important role on MKE in the region, for the former brings MKE to the region above the separation bubble and the latter convects MKE downward from the shear layer and above to the separation bubble. For the MKE budgets from different Reynolds numbers, similarities are in general observed at different locations downstream of the bubble center. At the beginning of the separation bubble (e.g., $1.5h$ upstream of the bubble center), the maxima of the MC and TC terms increase significantly with the increase in the Reynolds number, which plays a key role on the decrease in the size of the separation bubble.

DATA AVAILABILITY

The data that support the findings of this study are available from the corresponding author upon reasonable request.

REFERENCES

[1] U. Piomelli, "Wall-layer models for large-eddy simulations," Prog. Aerosp. Sci. **44**, 437–446 (2008).

[2] H. Choi and P. Moin, "Grid-point requirements for large eddy simulation: Chapman's estimates revisited," Phys. Fluids **24**, 011702 (2012).

[3] G. W. He, G. D. Jin, and Y. Yang, "Space-time correlations and dynamic coupling in turbulent flows," Annu. Rev. Fluid Mech. **49**, 51–70 (2017).

[4] S. T. Bose and G. I. Park, "Wall-modeled large-eddy simulation for complex turbulent flows," Annu. Rev. Fluid Mech. **50**, 535–561 (2018).

[5] L. Temmerman, M. A. Leschziner, C. P. Mellen, and J. Fröhlich, "Investigation of wall-function approximations and subgrid-scale models in large eddy simulation of separated flow in a channel with streamwise periodic constrictions," Int. J. Heat Fluid Flow **24**, 157–180 (2003).

[6] J. Fröhlich, C. P. Mellen, W. Rodi, L. Temmerman, and M. A. Leschziner, "Highly resolved large-eddy simulation of separated flow in a channel with streamwise periodic constrictions," J. Fluid Mech. **526**, 19–66 (2005).

[7] G. P. Almeida, D. F. G. Durão, and M. V. Heitor, "Wake flows behind two-dimensional model hills," Exp. Therm. Fluid Sci. **7**(1), 87–101 (1993).

[8] C. P. Mellen, J. Fröhlich, and W. Rodi, "Large eddy simulation of the flow over periodic hills," in 16th IMACS World Congress, Lausanne, Switzerland (2000).

[9] X. Han and S. Krajnović, "An efficient very large eddy simulation model for simulation of turbulent flow," Int. J. Numer. Meth. Fluids **71**, 1341–1360 (2013).

[10] B. Chaouat and R. Schiestel, "Hybrid RANS/LES simulations of the turbulent flow over periodic hills at high Reynolds number using the PITM method," Comput. Fluids **84**, 279–300 (2013).

[11] B. Kadoch, T. Reimann, K. Schneider, and M. Schäfer, "Comparison of a spectral method with volume penalization and a finite volume method with body fitted grids for turbulent flows," Comput. Fluids **133**, 140–150 (2016).

[12] R. Mokhtarpoor, S. Heinz, and M. Stoellinger, "Dynamic unified RANS-LES simulations of high Reynolds number separated flows," Phys. Fluids **28**, 095101 (2016).

[13] M. Breuer, B. Kniazev, and M. Abel, "Development of wall models for les of separated flows using statistical evaluations," Comput. Fluids **36**, 817–837 (2007).

[14] C. Duprat, G. Balarac, O. Métais, P. M. Congedo, and O. Brugière, "A wall-layer model for large-eddy simulations of turbulent flows with/out pressure gradient," Phys. Fluids **23**, 015101 (2011).

[15] B. Chaouat, "The state of the art of hybrid RANS/LES modeling for the simulation of turbulent flows," Flow Turbul. Combust. **99**, 279–327 (2017).

[16] M. Breuer, N. Peller, C. Rapp, and M. Manhart, "Flow over periodic hills—Numerical and experimental study in a wide range of Reynolds numbers," Comput. Fluids **38**, 433–457 (2009).

[17] B. Krank, M. Kronbichler, and W. A. Wall, "Direct numerical simulation of flow over periodic hills up to Re_h=10,595," Flow Turbul. Combust. **101**(2), 521–551 (2018).

[18] X. Gloerfelt and P. Cinnella, "Large eddy simulation requirements for the flow over periodic hills," Flow Turbul. Combust. **103**, 55–91 (2019).

[19] C. Rapp and M. Manhart, "Flow over periodic hills: An experimental study," Exp. Fluids **51**, 247–269 (2011).

[20] C. J. Kähler, S. Scharnowski, and C. Cierpka, "Highly resolved experimental results of the separated flow in a channel with streamwise periodic constrictions," J. Fluid Mech. **796**, 257–284 (2016).

[21] P. Balakumar, "DNS/LES simulations of separated slows at high Reynolds numbers," AIAA Paper No. 2015-2783 (2015).

[22] H. Xiao, J.-L. Wu, S. Laizet, and L. Duan, "Flows over periodic hills of parameterized geometries: A dataset for data-driven turbulence modeling from direct simulations," Comput. Fluids **200**, 104431 (2020).

[23]W. Gao, W. Cheng, and R. Samtaney, "Large-eddy simulations of turbulent flow in a channel with streamwise periodic constrictions," J. Fluid Mech. **900**, A43 (2020).

[24]J. Ziefle, S. Stolz, and L. Kleiser, "Large-eddy simulation of separated flow in a channel with streamwise-periodic constrictions," AIAA J. **46**, 1705–1718 (2008).

[25]Z. D. Zhou, G. W. He, and X. L. Yang, "Wall model based on neural networks for LES of turbulent flows over periodic hills," Phys. Rev. Fluids **6**, 054610 (2021).

[26]S. Song and J. Eaton, "Reynolds number effects on a turbulent boundary layer with separation, reattachment, and recovery," Exp. Fluids **36**, 246–258 (2004).

[27]H. Abe, "Reynolds-number dependence of wall-pressure fluctuations in a pressure-induced turbulent separation bubble," J. Fluid Mech. **833**, 563–598 (2017).

[28]H. Abe, "Direct numerical simulation of a turbulent boundary layer with separation and reattachment over a range of Reynolds numbers," Fluid Dyn. Res. **51**, 011409 (2019).

[29]G. N. Coleman, C. L. Rumsey, and P. R. Spalart, "Numerical study of turbulent separation bubbles with varying pressure gradient and Reynolds number," J. Fluid Mech. **847**, 28–70 (2018).

[30]X. L. Yang, F. Sotiropoulos, R. J. Conzemius, J. N. Wachtler, and M. B. Strong, "Large-eddy simulation of turbulent flow past wind turbines/farms: The Virtual Wind Simulator (VWiS)," Wind Energy **18**(12), 2025–2045 (2015).

[31]X. L. Yang and F. Sotiropoulos, "A new class of actuator surface models for wind turbines," Wind Energy **21**(5), 285–302 (2018).

[32]S. Kang and F. Sotiropoulos, "Numerical modeling of 3D turbulent free surface flow in natural waterways," Adv. Water Resour. **40**, 23–36 (2012).

[33]S. Kang, X. L. Yang, and F. Sotiropoulos, "On the onset of wake meandering for an axial flow turbine in a turbulent open channel flow," J. Fluid Mech. **744**, 376–403 (2014).

[34]A. Khosronejad and F. Sotiropoulos, "Numerical simulation of sand waves in a turbulent open channel flow," J. Fluid Mech. **753**, 150–216 (2014).

[35]X. L. Yang, A. Khosronejad, and F. Sotiropoulos, "Large-eddy simulation of a hydrokinetic turbine mounted on an erodible bed," Renewable Energy **113**, 1419–1433 (2017).

[36]X. L. Yang and F. Sotiropoulos, "On the dispersion of contaminants released far upwind of a cubical building for different turbulent inflows," Build. Environ. **154**, 324–335 (2019).

[37]X. L. Yang and F. Sotiropoulos, "Wake characteristics of a utility-scale wind turbine under coherent inflow structures and different operating conditions," Phys. Rev. Fluids **4**(2), 024604 (2019).

[38]D. Foti, X. L. Yang, L. Shen, and F. Sotiropoulos, "Effect of wind turbine nacelle on turbine wake dynamics in large wind farms," J. Fluid Mech. **869**, 1–26 (2019).

[39]A. Khosronejad, K. Flora, and S. Kang, "Effect of inlet turbulent boundary conditions on scour predictions of coupled LES and morphodynamics in a field-scale river: Bankfull flow conditions," J. Hydraul. Eng. **146**(4), 04020020 (2020).

[40]M. Germano, U. Piomelli, P. Moin, and W. H. Cabot, "A dynamic subgrid-scale eddy viscosity model," Phys. Fluids A **3**, 1760 (1991).

[41]L. Ge and F. Sotiropoulos, "A numerical method for solving the 3D unsteady incompressible Navier-Stokes equations in curvilinear domains with complex immersed boundaries," J. Comput. Phys. **225**(2), 1782–1809 (2007).

[42]S. Kang, A. Lightbody, C. Hill, and F. Sotiropoulos, "High-resolution numerical simulation of turbulence in natural waterways," Adv. Water Resour. **34**(1), 98–113 (2011).

[43]J. Jeong and F. Hussain, "On the identification of a vortex," J. Fluid Mech. **285**, 69–94 (1995).

[44]T. R. Troutt, B. Scheelke, and T. R. Norman, "Organized structures in a reattaching separated flow field," J. Fluid Mech. **143**, 413–427 (1984).

[45]Y. Na and P. Moin, "The structure of wall-pressure fluctuations in turbulent boundary layers with adverse pressure gradient and separation," J. Fluid Mech. **377**, 347–373 (1998).

[46]J. Kim, P. Moin, and R. Moser, "Turbulence statistics in fully developed channel flow at low Reynolds number," J. Fluid Mech. **177**, 133–166 (1987).